USGS
science for a changing world

$^{40}Ar/^{39}Ar$ Geochronology of Hypabyssal Igneous Rocks in the Marañon Basin of Peru—A Record of Thermal History, Structure, and Alteration

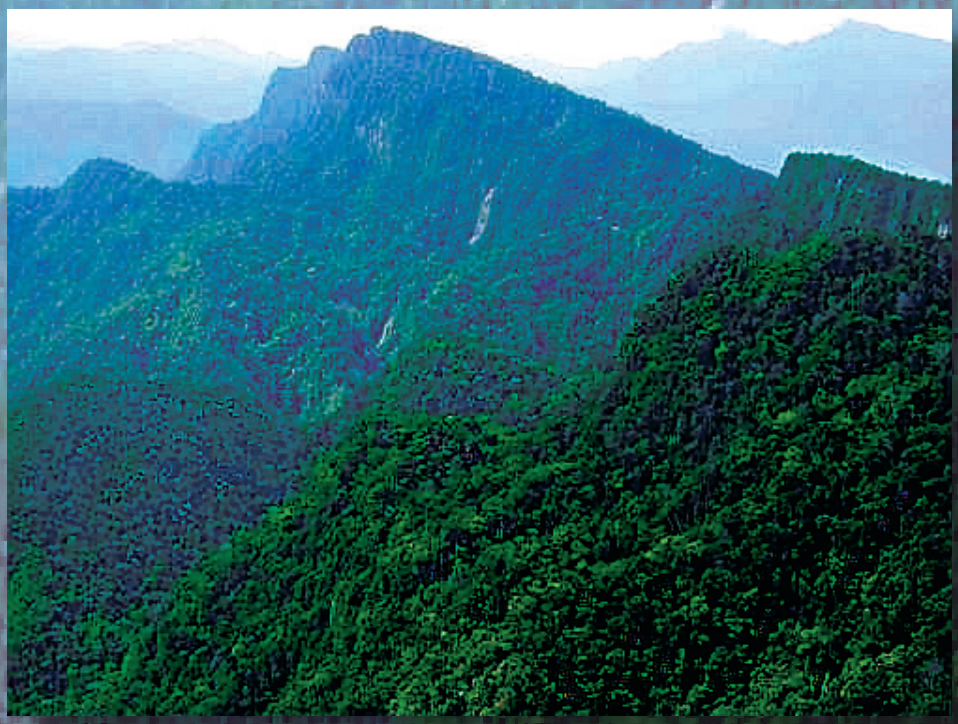

Scientific Investigations Report 2005-5132

U.S. Department of the Interior
U.S. Geological Survey

$^{40}Ar/^{39}Ar$ Geochronology of Hypabyssal Igneous Rocks in the Marañon Basin of Peru—A Record of Thermal History, Structure, and Alteration

By L.M Prueher, R. Erlich, and L.W. Snee

Scientific Investigations Report 2005–5132

U.S. Department of the Interior
U.S. Geological Survey

U.S. Department of the Interior
Gale A. Norton, Secretary

U.S. Geological Survey
P. Patrick Leahy, Acting Director

U.S. Geological Survey, Reston, Virginia: 2005

For product and ordering information:
World Wide Web: http://www.usgs.gov/pubprod
Telephone: 1-888-ASK-USGS

For more information on the USGS--the Federal source for science about the Earth,
its natural and living resources, natural hazards, and the environment:
World Wide Web: http://www.usgs.gov
Telephone: 1-888-ASK-USGS

Suggested citation:
Prueher, L.M., Erlich, R., and Snee L.W., 2005, $^{40}Ar/^{39}Ar$ geochronology of hypabyssal igneous rocks in the Marañon Basin of Peru—A record of thermal history, structure, and alteration: U.S. Geological Survey Scientific Investigations Report 2005–5132, 41 p.

Contents

Appendixes

Figures

Tables

$^{40}Ar/^{39}Ar$ Geochronology of Hypabyssal Igneous Rocks in the Marañon Basin of Peru—A Record of Thermal History, Structure, and Alteration

By L.M Prueher,[1] R. Erlich,[2] and L.W. Snee[1]

Abstract

Hypabyssal andesites and dacites from the Balsapuerto Dome in the Marañon Basin of Peru record the thermal, tectonic, and alteration history of the area. The Marañon Basin is one of 19 sub-Andean foreland basins. The hypabyssal rocks in the Balsapuerto Dome are one of four known occurrences of subvolcanic rocks along the deformation front in Peru. This dome is a potential petroleum structural trap. Petroleum seeps near the dome indicate that a source for the petroleum is present, but the extent and amount of petroleum development is unknown.

The Balsapuerto hypabyssal rocks are plagioclase-, hornblende-, pyroxene-phyric andesites to dacites. Some parts of the dome are pervasively altered to a hydrothermal assemblage of quartz-sericite-pyrite. $^{40}Ar/^{39}Ar$ geochronology shows that thermal activity related to emplacement of these subvolcanic rocks took place between 12–10 Ma, subsequent to the major periods of Andean folding and faulting, previously assumed to have occurred about 9 Ma. Eleven argon mineral age-spectrum analyses were completed. Argon apparent ages on amphibole range from 12.7 to 11.6 Ma, and the age spectra are simple, which indicates that the ages are very close to emplacement ages. Potassium feldspar yields an argon age spectrum ranging in age from 12.5 to 11.4 Ma, reflecting the period during which the potassium feldspar closed to argon diffusion between the temperature range of 350°C to about 150°C; thus the potassium feldspar age spectrum reflects a cooling profile throughout this temperature range. This age range is consistent with ages of emplacement for the entire igneous complex indicating that an increased thermal state existed in the area for at least 1.0 m.y. Combined with the coexisting hornblende age, this rock cooled from ~580°C to ~150°C in ~1.2 m.y. resulting in an average cooling rate of 358°C /m.y. White mica, or sericite, formed as a later alteration phase associated with quartz- sericite- pyrite and propylitic alteration in some samples. Three age-spectrum analyses on white mica indicate that alteration occurred at 12.5 Ma and again at 11 Ma, and suggest that alteration fluids were present throughout the range of emplacement and as long as 0.5 m.y. afterward.

Based on these data, emplacement of the intrusive body(ies) began at about 12.7 Ma. The hornblende age range can be interpreted to reflect multiple periods of intrusion from 12.7 to 11.6 Ma or a period of thermal activity and high-temperature cooling during this age range. The potassium feldspar cooling age range supports either interpretation. The white mica ages indicate that at least two periods of hydrothermal activity occurred at 12.5 and 11.0 Ma, throughout the period of emplacement and cooling of the intrusive body below about 150°C. The magmatic and hydrothermal systems were active after the intrusion, with temperatures not reaching 150°C until about 1 m.y. after emplacement. Therefore, the thermal effects associated with emplacement of the intrusion and the associated hydrothermal system were probably high enough to destroy petroleum in the host and source rocks. Thus, the Balsapuerto Dome is not a viable source of petroleum. There is no evidence in the rock samples or thin sections for brittle or ductile deformation suggesting that this body was emplaced in its present location after cessation of Andean thrusting. Andean thrusting had been assumed to end about 9 Ma. However, this new data suggested that the Andean thrusting had ceased by about 12–10 Ma.

Introduction

The Marañon Basin of Peru is one of 19 sub-Andean foreland basins located between the Andes Mountains and the Brazilian Shield (fig. 1). The formation of the present Marañon Basin is related to oblique, east-directed convergence between the Nazca and South American plates.

Sub-Andean basins have been the subject of extensive study for the past 75 years, due at least in part to the large volumes of hydrocarbons found in them. The Balsapuerto Dome is a potential petroleum structural trap cored by shallowly emplaced subvolcanic (hypabyssal) rocks. Petroleum seeps near the dome indicate that a source for the petroleum is present, but the extent and amount of petroleum development

[1]U.S. Geological Survey, Box 25046, MS 974, Denver Federal Center, Denver, CO 80225-0046.

[2]Burlington Resources, 717 Texas Avenue, Suite 2100, Houston, TX 77002-2712.

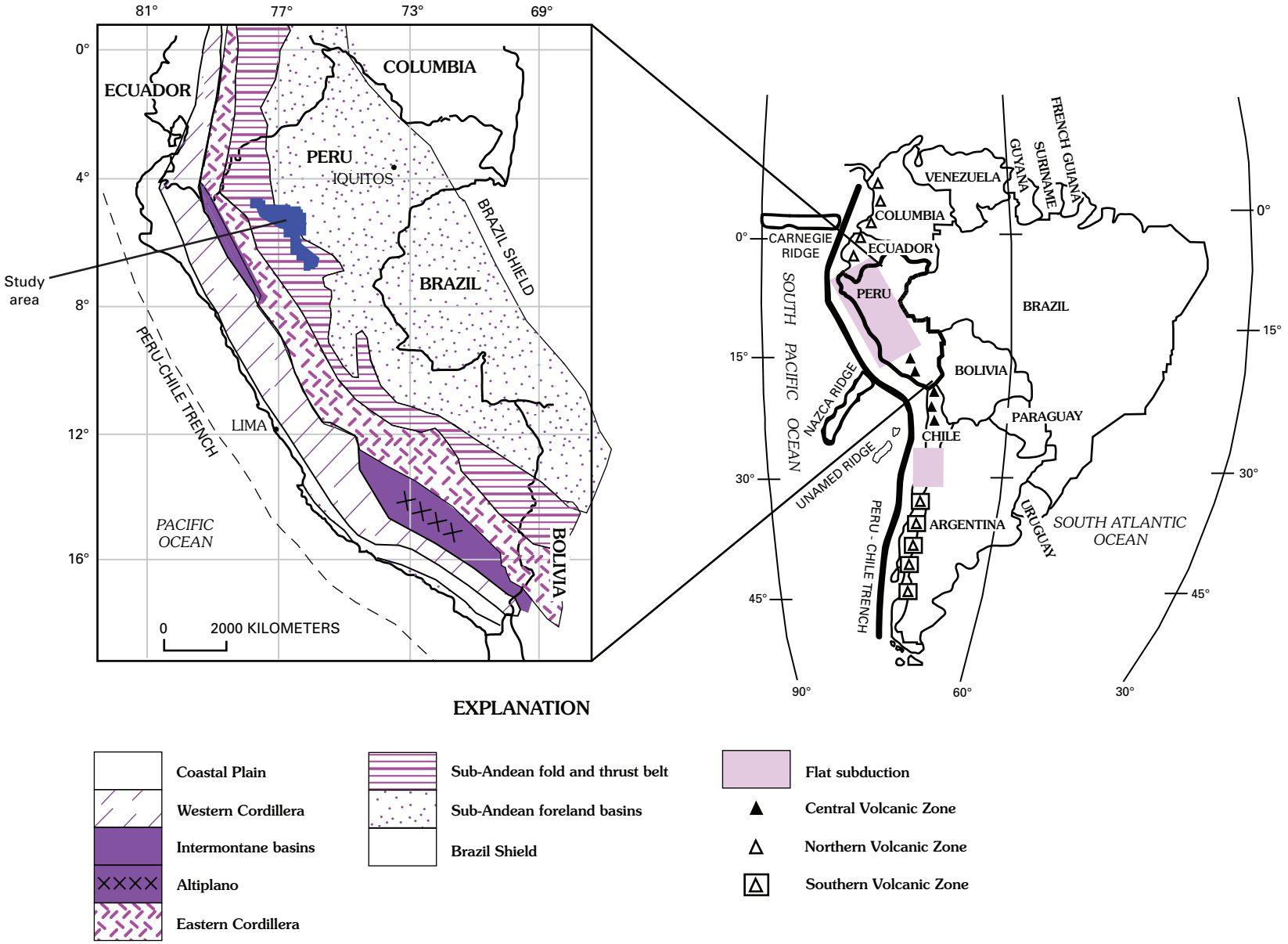

Figure 1. Map of South America showing Peru, volcanic zones, flat subduction segments (after James and Sacks, 1999), Carnegie and Nazca Ridges and unnamed ridge, and location of Peru-Chile trench. Inset shows map of Peru with tectonic divisions. Modified tectonic boundaries after Jaillard and others (2000) and Benavides-Cáceres (1999).

is unknown. Of critical importance for evaluation of the petroleum resource potential within the dome is to determine if the hypabyssal rocks were emplaced before or after thrusting in the Andean fold and thrust belt. If the igneous rocks within the dome are older than the cessation of Andean thrusting, they are likely allocthonous and were structurally emplaced with the dome during regional thrusting. This possibility is encouraging for petroleum resource potential. In contrast, if the igneous rocks are younger than the regional structural events, then they likely were emplaced into the foreland sedimentary sequence forming the dome. This possibility is less attractive from the standpoint of petroleum resource potential because thermal effects associated with emplacement may have been sufficiently high enough to destroy petroleum in the host and source rocks. Alternatively, if the thermal effects were minimal, then only local baking may have occurred.

The study area in the southwestern part of the Marañon Basin is centered on the Balsapuerto Dome, an area long recognized as a center of intrusive igneous activity (Stewart, 1971; fig. 2). In the past, the presence of igneous rocks east of the sub-Andean fold and thrust belt and within the sub-Andean basins has attracted interest because it is so far inland, approximately 3,000 km, from the present subduction zone, and there are few instances of this type of activity in Peru (fig. 1). Previous authors (Sébrier and Soler, 1991; Benavides-Cáceres, 1999; James and Sacks, 1999) assumed an age for the Balsapuerto Dome of 5–4 Ma, based on the work of Stewart (1971), and that the rocks are peralkaline in composition. However, the current study shows the rocks to be 12–10 Ma and andesitic to dacitic in composition with no petrographic evidence of peralkalinity.

Regional Geology

The major geologic provinces of Peru (fig. 1) are, from west to east, the Peru-Chile trench, the Coastal Plain, the Western Cordillera, the intermontane basins (Altiplano of southern Peru), the Eastern Cordillera, the sub-Andean fold and thrust belt, where most of the deformation is occurring today (James and Sacks, 1999), the sub-Andean foreland basins, and the Brazilian Shield. Active volcanoes occur in the Western Cordillera in southern Peru (also known as the Central Volcanic Zone; fig. 1). North of the Central Volcanic Zone there is a gap—an area of no active volcanism. Active volcanism continues north into Ecuador where it is part of the Northern Volcanic Zone.

The Andes are segmented into areas of flat-slab subduction and normal subduction (fig. 1). These segments can be delineated by deflections—areas where the trend of the Andes changes. Tectonic, volcanic, and structural features within a given segment are controlled not only by the segmentation of the downgoing slab, but also by basement features and sediments of the overriding plate that give rise to thin- and thick-skinned tectonic features (Mathalone and Montoya, 1995; James and Sacks, 1999; Kley and others, 1999; Ramos and Aleman, 2000). Gaps in active volcanism occur over areas where the subduction angle of the down-going slab is relatively flat.

The Andean segments have been named by multiple authors. In this paper, we use the naming convention proposed by Ramos and Aleman (2000), James and Sacks (1999), and Jordan and others (1983). The flat-slab segments are between 2°S. and 15°S. and 27°S. and 33°S. (fig. 1). Megard (1989) added a fourth deflection, the Cajamarca deflection, at 8°S.

Three such deflections occur in Peru (fig. 2): the Huancabamba deflection at about 3°S., the Abancay deflection at about 13°S. (Dunbar and others, 1990; Benavides-Cáceres, 1999), and the Arica elbow at about 18°S. (Jaillard and others, 2000). The Abancay deflection is also known as the Pisco deflection (Mégard, 1989; James and Sacks, 1999). The flat-slab segment in Peru begins at the Huancabamba deflection and extends south, past the Abancay deflection to about 15°S., at which point volcanism begins again.

Although the slab is referred to as a flat slab, the subduction angle is actually greater than 0°. Reported angles in the literature vary from a dip of 5°–10° (Jordan and others, 1983) to horizontal (James and Sacks, 1999). The proximity of the Nazca and Juan Fernandez Ridges to areas of flat-slab subduction (fig. 1) suggests that the subduction of these ridges is responsible for the flattening of the dip angle. In the central Andes, the steepening of the slab dip toward the east may be caused by impingement of the downgoing slab against the western margin of the Brazilian Shield (Kley and others, 1999).

Sub-Andean Basins

Many sub-Andean basins have undergone three main stages of Cenozoic compressional deformation. Previous authors named the deformational events the Quechua I, II, and III deformations (table 1). As in other parts of the Andes, along-strike as well as across-strike variations in deformation occur. Different deformational events were manifested in the basins at slightly different times. For this reason, some authors choose not to use the Quechua designation but refer to the deformation by age (see, for example, Jordan and others, 1983; Sébrier and Soler, 1991; James and Sacks, 1999) or phase. We will follow this second convention, naming the three main deformations Phase I, II, and III (table 1), and include a brief summary of the events. Phase III is discussed in greater detail because it had the most impact on the Marañon Basin.

Phase I—(Pre-Quechua) Triassic to Paleocene

The first phase of deformation occurred prior to the initiation of Quechua I tectonism (table 1) and affected the pre-existing Paleozoic rocks. Phase I deformation occurred in a back-arc setting, and extensional stresses produced reactivation of older faults (Benavides-Cáceres, 1999; Jaillard and others, 2000). Triassic–Paleocene sediments were deposited upon eroded Paleozoic rocks. This deformation is associated with cessation of Pacific-Farallon spreading and the ensuing ridge jump (Benavides-Cáceres, 1999).

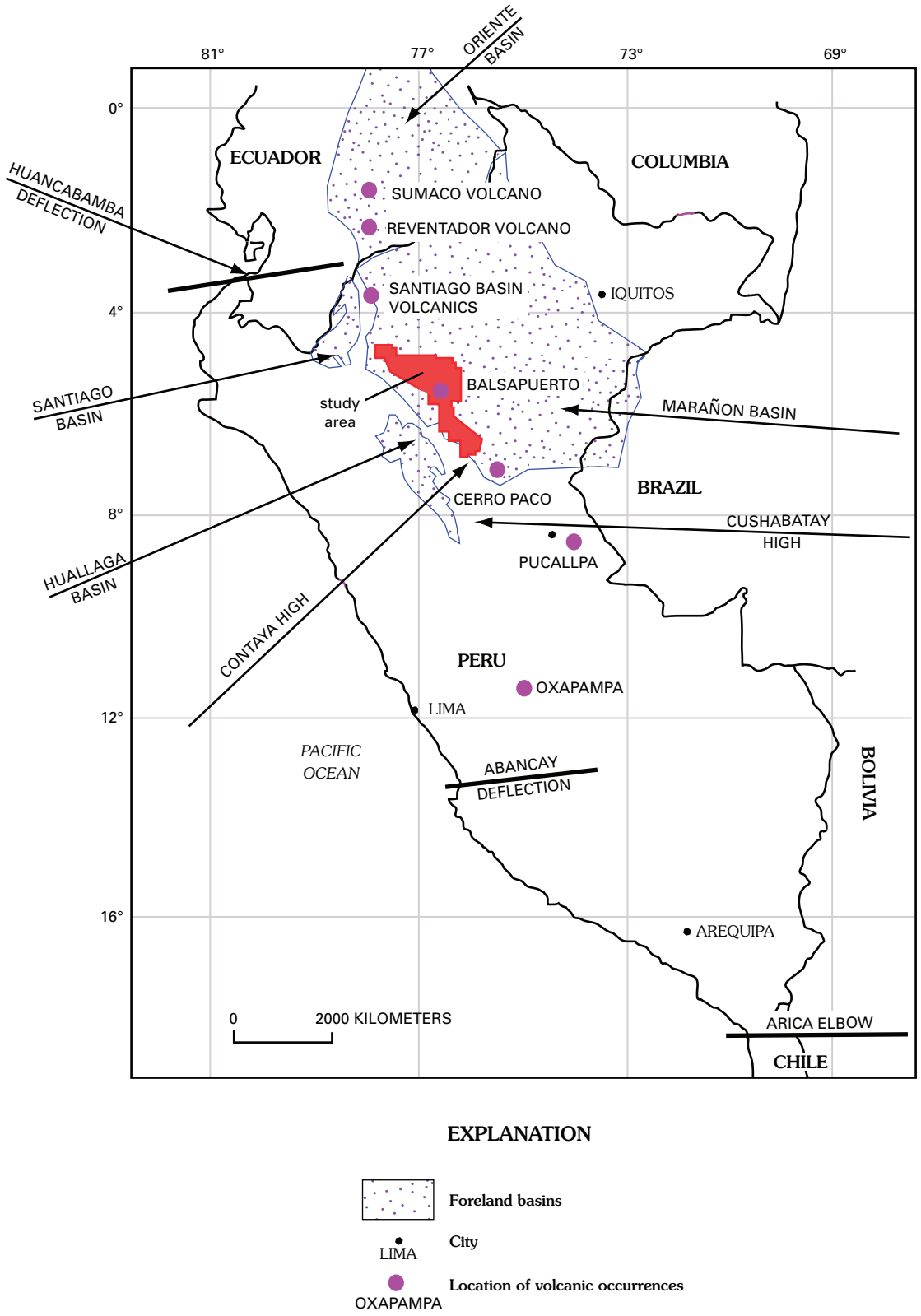

Figure 2. Locations of deflections and sub-Andean volcanic and subvolcanic activity in Peru and Ecuador. Study area is also shown. Location of volcanic occurrences after Sebriér and Soler (1991) and Stewart (1971). Basin outlines after Wine and others (2003) and Mathalone and Montoya (1995).

Table 1. Names and ages of Cenozoic compressional events in Peru.

This paper	Equivalent events	Jaillard and others (2000)	Benavides-Caceres (1999)	Mathalone and Montoya (1995)
Phase I	pre-Quechua			
Phase II	Quechua I	17–15 Ma	17 Ma	Oligocene–Miocene
Phase II	Quechua II	9–8 Ma	8–7 Ma	mid-Miocene
Phase III	Quechua III	7–5 Ma	5–4 Ma	mid-Miocene to Pliocene

Phase II—(Corresponds to Quechua I and II) Oligocene to Miocene

The second phase of structural development varied greatly along the trend of sub-Andean basins, but generally involved a combination of compressive structural deformation and sedimentary tectonics. These two processes were closely linked in northern South America (shale diapirism in Colombia-Venezuela-Trinidad) but were initially distinct in Peru. This difference is highlighted by the early salt pillowing and associated structural deformation observed in the Ucayali and southwestern Marañon Basins, which occurred in those areas in the Jurassic and Late Cretaceous–early Paleogene, respectively. The intermontane basins, the sub-Andean fold and thrust belt, and the sub-Andean foreland basins formed during this phase (Benavides-Cáceres, 1999; Jaillard, and others, 2000), possibly as a result of the eastward thrusting of pre-Cretaceous rocks over the Guiana and Brazilian Shields.

Phase III—(Corresponds to Quechua III) Miocene to Pliocene

The third phase of deformation that occurred in the sub-Andean basins was an evolution from compressive, thrust-dominated deformation to inversion and basement uplift. Subsidence and deformation continued in the foreland basins (Benavides-Cáceres, 1999; Jaillard and others, 2000) and is related to the subduction of the Nazca and Carnegie Ridges (Jaillard and others, 2000).

The deformation style of the central Andean Cordillera reflects the interaction of plate margin compressive stresses on a complex of competent basement rocks. Variations in lithospheric temperatures away from the central Andean core alternately produced thin-skinned, long run-out detachments followed by thick-skinned high-angle basement inversions. These later faults can have vertical uplifts of >5,000 m with only minor lateral offsets observed from outcrop (generally <1,000 m).

Structural Development of the Marañon Basin

The Marañon Basin (figs. 2 and 3) formed in the Early Triassic and is part of the Marañon-Oriente-Putumayo Basin that extends from Columbia to Peru (Mathalone and Montoya, 1995). Post-Paleozoic deformation of the basin began in the Triassic–Early Jurassic with passive margin subsidence and reactivation of Paleozoic faults as half grabens and back-arc extension. Back-arc rifting and half-graben development were reinitiated during the Late Jurassic but abruptly ceased during the Early Cretaceous. Passive margin subsidence characterized the remainder of Cretaceous through Paleocene history of the Marañon Basin. Late Cretaceous–late Miocene doming of Triassic–Jurassic salt bodies occurred on the flanks of uplifted basement highs, primarily in response to differential compaction and sedimentation along the western basin margin.

The shift from dominantly passive margin/back-arc to dominantly active margin foreland subsidence in the Marañon Basin occurred during the late Eocene–early Miocene with incipient overthrusting of the Andes toward the east–northeast. Minor igneous intrusive activity, commonly observed in foreland basins, can also be observed in the Balsapuerto area and other parts of Peru, and occurred during the middle Miocene (fig. 2). A reversal in vergence direction located along the southern boundary of the Santiago Basin also occurred at this time and is coincident with the Amazonas megashear. From this point north to the Ecuadorian border, thrust faults dip mostly toward the east as opposed to the normal Andean west dipping thrusts.

Thin-skinned deformation, as opposed to the thick-skinned deformation of the central Andean Cordillera, was the dominant deformation style until the Pliocene in the Huallaga and Marañon Basins. The thin-skinned deformation reflects the effective transference of compressive stress toward the east–northeast. However, inversion of pre-existing Paleozoic and Jurassic half-grabens also occurred in a southwest–northeast progression, as compressive stress was transferred into pre-existing foreland basins.

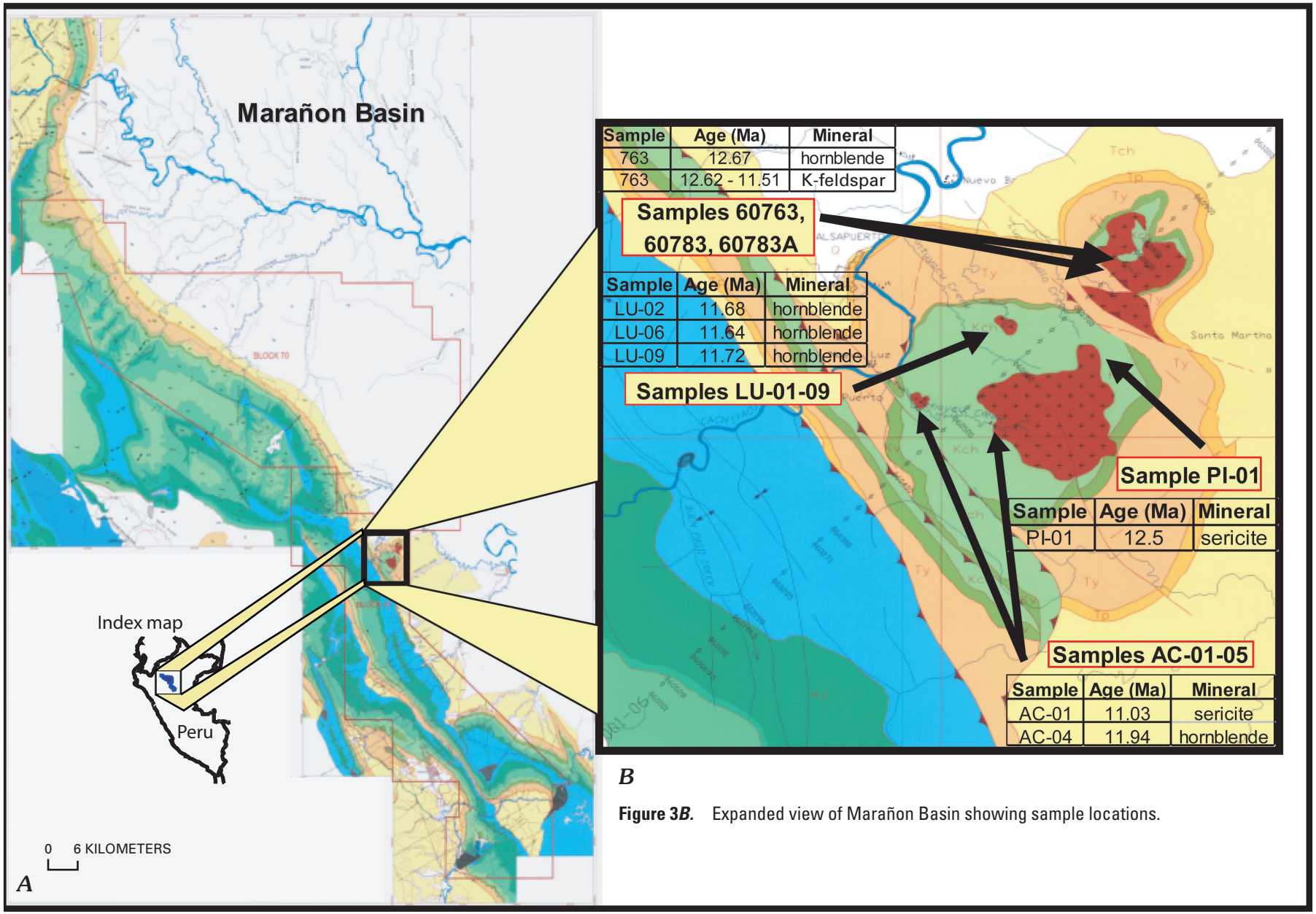

Figure 3*A*. Index map of Marañon Basin.

Figure 3*B*. Expanded view of Marañon Basin showing sample locations.

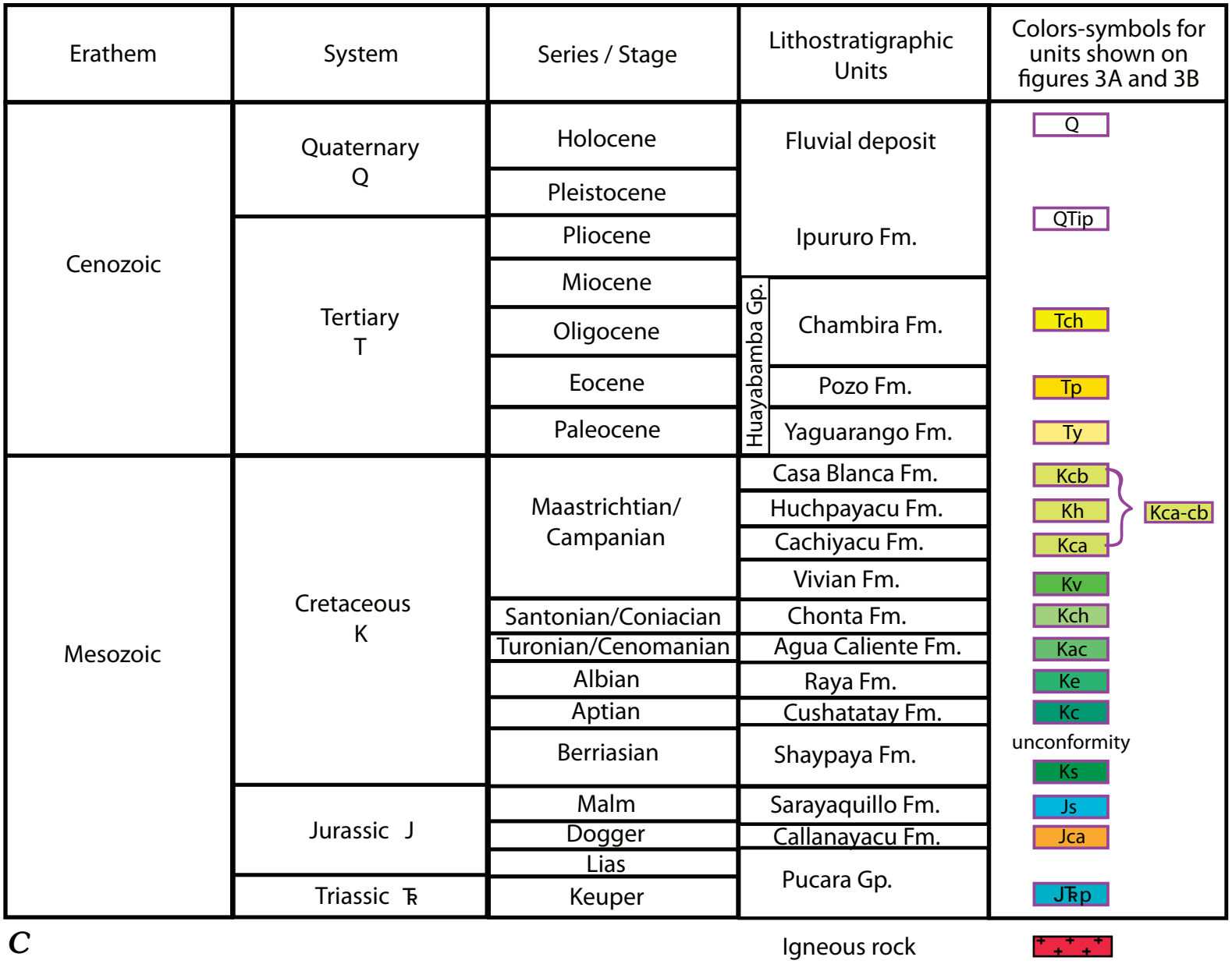

C

Figure 3*C*. Stratigraphic column of Marañon Basin.

Inversion of pre-existing normal faults occurred in the study area during the late Eocene–early Miocene and initially impacted basement uplifts on their western and southwestern flanks. Late Miocene–Pliocene compressive deformation culminated in thrusts that initially overrode the basement and salt-induced uplifts, but were beheaded during the Pliocene by high amplitude inversion and uplift of the basement arches.

Asymmetric uplift of the Chazuta-Contaya-Cushabatay arch occurred during the late Miocene–Pliocene, and may be due in part to lithospheric cooling in the central Andean core and late reactivation of the older Contaya-Cushabatay wrench fault system (fig. 2). This uplift resulted in the separation of the Santiago and Huallaga Basins from the Marañon Basin. The western part of the area was uplifted to a greater elevation than the eastern part. However, reactivation of ramps within the thrust belt was minimal, because most thrusts were locked and already buttressed against basement uplifts. Locking of the thrust belt resulted in the development of backthrusting in the Marañon Basin, which becomes progressively younger toward the northeast.

Structurally, the Marañon Basin can be divided into two distinct parts, western and eastern. The western part is older and exhibits different response to deformation. Toward the west, near the central Andean Cordillera, thrust belt anticlines have higher amplitudes, shorter wavelengths, and translation distances of 1–10 km. These features formed in the late phases of compressive Andean tectonics. More distal thrusts, such as those in the study area, are somewhat older and have much more significant displacements, some on the order of 40 km. The inversion and reactivation of Paleozoic structures are more pronounced in the eastern part of the basin, which was more affected by the mid-Miocene to Pliocene or Quechua III deformational event (Mathalone and Montoya, 1995; Wine and others, 2003).

Sub-Andean Igneous Rocks

Hypabyssal igneous rocks outcrop in the sub-Andean region of northern and central Peru (table 2). Previous authors considered the rocks to be Pliocene in age and alkaline (Stewart, 1971) to peralkaline in composition (Stewart, 1971; Sébrier and Soler, 1991; Sandeman and others, 1997; Benavides-Cáceres, 1999; James and Sacks, 1999). The rocks of the Balsapuerto Dome fall into this group of rocks.

Stewart (1971) described four occurrences of hypabyssal volcanism in northern and central Peru: phonolite plugs near Pucallpa, a porphyry near Cerro Paco, the Balsapuerto Dome, and plugs in the Santiago Basin (table 2; fig. 2). The four intrusions are aligned along a linear trend and may be related (fig. 2; Stewart, 1971). However, a definite correlation between these rocks cannot be made without information on the geochemistry of the four intrusions. Geochemical analyses of the Balsapuerto rocks are underway. However, there is a lack of geochemical data for the Cerro Paco and Santiago rocks.

K/Ar age determinations for the Pucallpa rocks show the samples to be Miocene in age. Cryptoperthite phenocrysts from the Pucallpa phonolites yielded K/Ar ages of 4.5–5 m.y. Cryptoperthite has multiple argon closure domains, so these ages must be considered as minimum ages. The samples are assumed to have an age between 5 m.y. and post late Miocene (Stewart, 1971).

Two other occurrences of alkaline rocks have been included in this group: the Yanachaga batholith near Oxapampa, and Sumaco and Reventador Volcanoes in the Oriente Basin in Ecuador (fig. 2; table 2). The Yanachaga batholith (table 2), located in the Eastern Cordillera, is alkalic (Benavides-Cáceres, 1999), Miocene in age, and also was produced in a back-arc environment. Nephelinic and alkalic syenite stocks to the east of Oxapampa show an age of 14 Ma (Soler and Bonhomme, 1988). The syenite stocks east of Oxapampa show evidence for a fractional crystallization of a partial melt of subduction-modified mantle (Sébrier and Soler, 1991). The Ecuadorian volcanoes are included because they are on the same trend, in the back-arc, and are alkaline in composition. Sumaco Volcano shows low LIL/HFS (large ion lithophile/high field strength) ratios, indicative of a small slab contribution and small amounts of partial melting (Talenti, 1994; Bourdon and others, 2003). Reventador Volcano is located northwest of Sumaco. Benavides-Cáceres (1999) noted it lies along a similar trend as that of Sumaco and stated that both volcanoes form a volcanic belt. However, petrologic data (Pichler and others, 1976) indicate that Reventador is calc-alkaline in composition and not similar in composition to Sumaco. Regardless of location, the composition of the sub-Andean igneous rocks exhibit the chemical characteristics of magma generated in a back-arc environment, such as evidence of crustal and (or) slab component and modification of the mantle source.

The fact that these rock bodies are all presumed to have an age similar to that of the Pucallpa samples has been used to support the idea that the deformation of the sub-Andean belt occurred between approximately 10 and 8 Ma (Benavides-Cáceres, 1999), because the intrusions postdate the deformation. Our data show that the Balsapuerto rocks are not 4.5–5 Ma in age but are older, with an age of 10–12 Ma. Petrographic work suggests the Balsapuerto rocks are neither alkaline nor peralkaline. Geochemical analyses are underway to determine the chemistry of the samples. The age discrepancies need to be resolved for the sub-Andean hypabyssal rocks, and the age of deformation and the relationship between the intrusions and the deformation need to be reconsidered.

Geology and Sample Locations

The general geology of the Balsapuerto area is displayed within the context of the regional geology of the eastern Andean fold and thrust belt on fig. 3*A*. The study area straddles the eastern edge of the Miocene-age fold and thrust belt where

Table 2. Occurrences of hypabyssal igneous rocks in Peru.

Location	Rock Type	Age	References	Other
Pucallpa–Brazil border	Phonolite plug	4.5–5 Ma >5 Ma or post late Miocene	Stewart (1971) Benavides-Cáceres (1999)	K/Ar age on cryptoperthite
Cerro Paco, Cushabatay region	Porphyry	Post-Miocene	Kummel (1948), Stewart (1971)	
Balsapuerto Dome	Andesite to dacites	1. 4.5 Ma 2. 10–12 m.y.	1. Benavides (1967) *in* Stewart (1971), Sébrier and Soler (1991), Benavides-Cáceres (1999) 2. This paper	2. Ar/Ar ages
Santiago Basin	Plug	Tertiary	Benavides (1967) *in* Stewart (1971), Benavides-Cáceres (1999)	
North of Oxapampa	Yanachaga batholith, alkalic, diorite	Mid-Miocene, 14 Ma	Soler and Bonhomme (1988), Sébrier and Soler (1991), and Benavides-Cáceres (1999)	K/Ar age
Ecuadorian volcanoes 1. Sumaco 2. Reventador	1. Peralkaline 2. Calc-alkaline	1. Holocene 2. Holocene	1. Stewart (1971), Benavides-Cáceres (1999) 2. Pichler, Hoermann and Braun (1976), Benavides-Cáceres (1999)	

Table 3. Sample locations, Balsa prospect, Peru.

Sample no.	Latitude (°S.)	Longitude (°W.)
AC01	5.87537	76.51434
AC02	5.87564	76.51665
AC03	5.87617	76.51917
AC04	5.86978	76.54041
AC05	5.86987	76.54207
60763	5.83097	76.4898
60783	5.82792	76.48678
60783A	5.82804	76.4863
PI01	5.85782	76.51213
LU01	5.84432	76.51855
LU02	5.84435	76.51778
LU03	5.84485	76.51691
LU04	5.84518	76.51652
LU05	5.84531	76.5161
LU06	5.84538	76.51589
LU07	5.84516	76.51904
LU08	5.84577	76.51911
LU09	5.84659	76.51926
LU10	5.84591	76.51813

the thrust belt appears to cut the western edge of an igneous rock-cored structural dome. In this area, Jurassic through Cretaceous sedimentary formations are thrust over sedimentary rocks as young as late Eocene through early Miocene (Chambira Formation). The Balsapuerto Dome exposes uplifted Cretaceous, Paleocene, and Eocene formations that are cross cut by hypabyssal andesitic to dacitic porphyritic rocks. Clearly the andesites to dacites are younger than the Eocene Pozo Formation, which they intrude, but the temporal relationship between the emplacement of the intrusive rocks and formation of nearby thrust faults is uncertain. Shown on fig. 3*B* are the five general areas from which 19 samples of intrusive rock were collected. Detailed maps of these collection areas are shown on figures 4, 5, and 6 with the areas of each indicated on fig. 3*B*. Sample locations are given in table 3.

Hand-Sample and Petrographic Description

The 19 samples range from generally unaltered, porphyritic, aphanitic, igneous rocks to highly altered rocks that retain textural resemblance to the unaltered samples. (Table 4 is a compilation of hand-specimen descriptions for the 19 samples; table 5 summarizes thin-section descriptions. Detailed

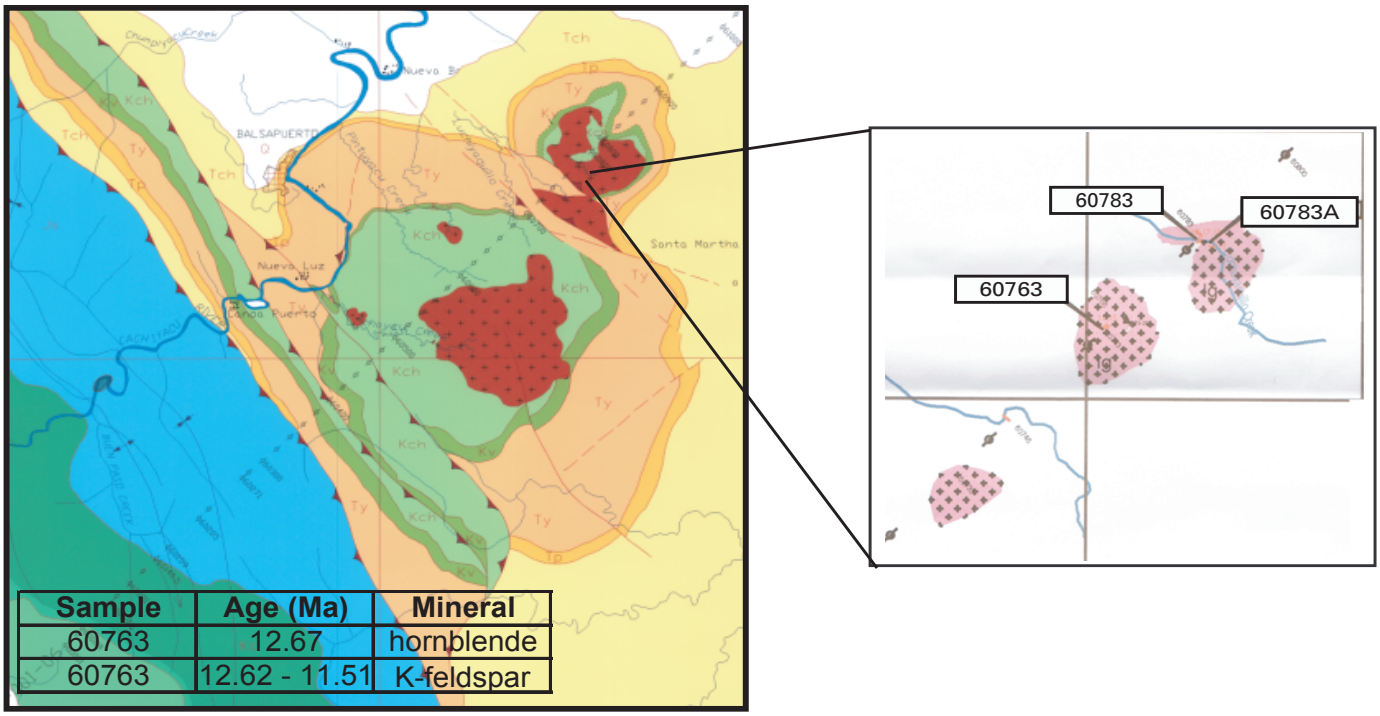

Figure 4. Sample locations for samples 60763 and 60783. Map units defined in figure 3*C*.

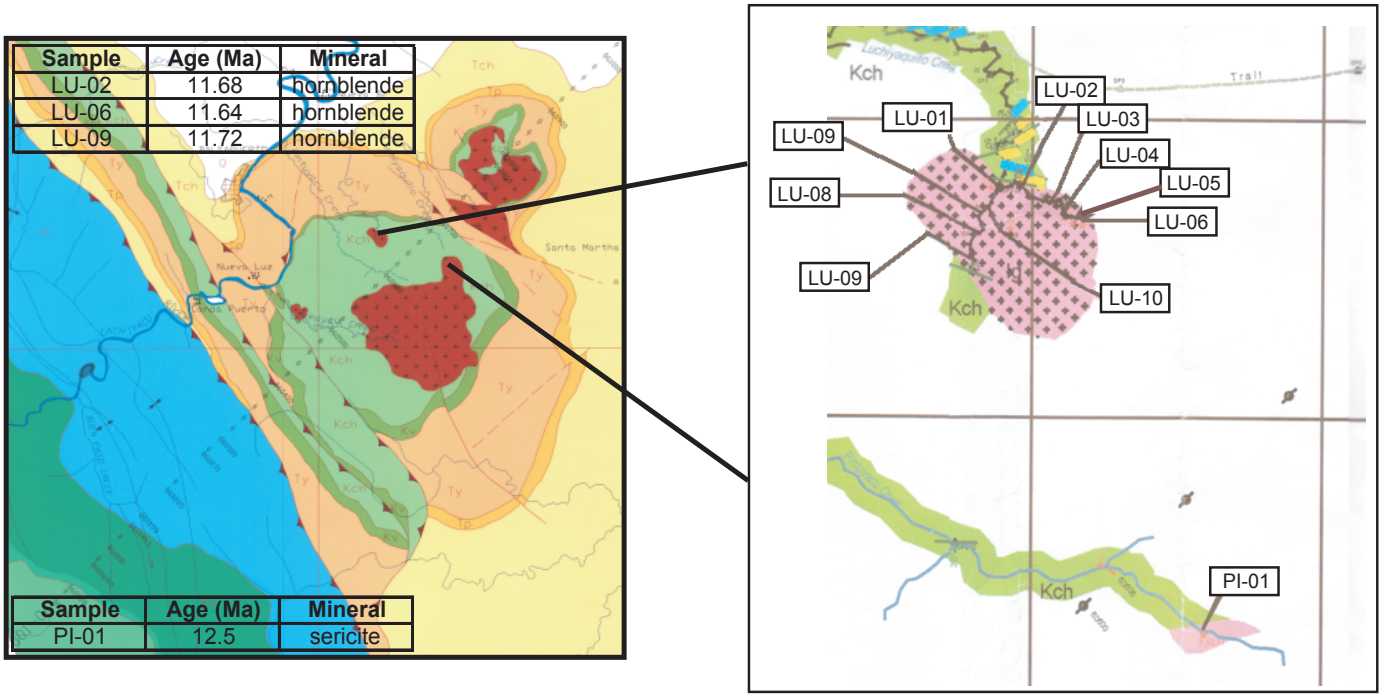

Figure 5. Sample locations for samples LU-01 to LU-10 and PI-01. Map units defined in figure 3*C*.

descriptions of each sample are in appendix 1; photomicrographs in appendix 2.) Unaltered rocks consist of between 20 and 40 percent phenocrysts ranging to as much as 7 mm in length in a fine-grained groundmass. In thin section, the phenocrysts are predominantly euhedral to subhedral plagioclase (oligoclase to andesine composition) with abundant amphibole, pyroxene, and iron oxide; lesser amounts of sphene and apatite; and minor potassium feldspar and quartz. Unaltered amphibole is hornblende, which is generally euhedral, green and twinned, and commonly displays oxyhornblende rims. Pyroxene is euhedral to subhedral, twinned augite. The groundmass ranges from felted, interlocking, fine-grained quartz and feldspar to pilotaxitic plagioclase microlites. In most samples, iron oxides are present as microlites, and in a few samples pyroxene microlites are present. In some cases, miarolitic cavities are evident and some vugs are filled with carbonate and xeolites. Compositionally, the rocks are andesites to dacites and texturally resemble subvolcanic intrusions.

The alteration in some samples (for example, AC01 and AC03) is pervasive and consists of variable amounts of carbonate, chlorite, sericite, pyrite, iron oxide, and quartz. Phenocrysts are pseudomorphs in the most altered samples. Veinlets of carbonate cut some samples (for example, AC02, LU02, and LU04). The alteration resembles a hydrothermal quartz-sericite-pyrite assemblage and records the addition of potassium, silica, sulfur, and carbonate to the rocks.

Geochronology

Methods

Sample ages were determined by the $^{40}Ar/^{39}Ar$ age-spectrum technique. The $^{40}Ar/^{39}Ar$ dating technique is a variant of the conventional K-Ar method and is based on the formation of ^{39}Ar during irradiation of potassium-bearing samples in a nuclear reactor. Using this nuclear reaction, the potassium content of the sample is relatively known and is used to constrain the amount of ^{40}K that decayed to ^{40}Ar throughout geologic time. To obtain a date by this technique, a sample of unknown age and a standard of known age are irradiated together to produce ^{39}Ar from ^{39}K by fast-neutron bombardment. Argon and contaminant gases are released from samples by step-wise (incremental) heating in an ultra-high vacuum furnace. After the gases are cleaned in various reactant devices (SAES getters), the argon isotopes are analyzed in a highly precise mass spectrometer. The result of the isotopic analysis is compared to the argon isotopic composition of a standard. The determination of a sample's age is based on the comparison of the sample's ^{39}Ar and ^{40}Ar to those of the standard of known age. The age is directly proportional to the $^{40}Ar/^{39}Ar$ ratio of the sample. For each sample, a series of dates results that potentially reveals information about the distribution of argon within the sample.

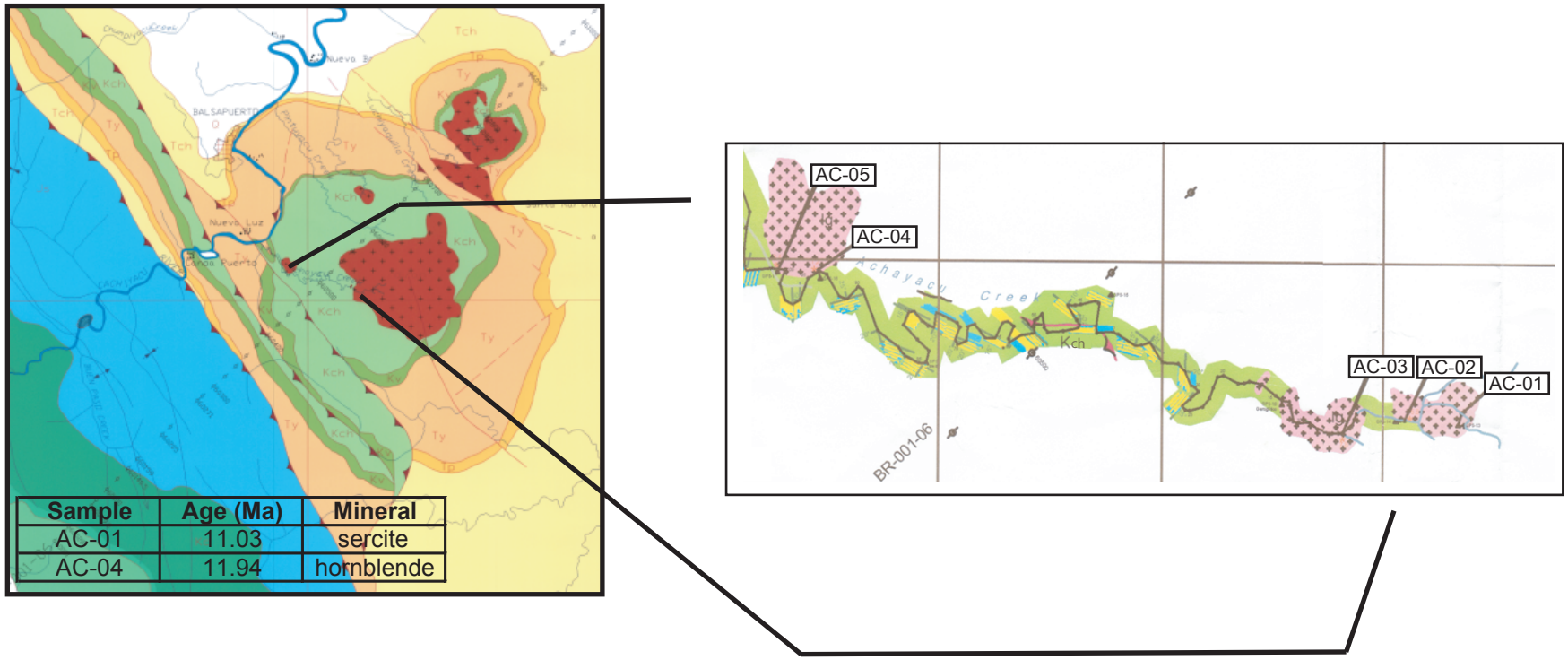

Figure 6. Sample locations for samples AC-01 to AC-05. Map units defined in figure 3*C*.

Table 4. Hand sample descriptions, Balsa prospect, Peru.

Sample no.	Sample description
AC01	Flow foliated, porphyritic, primary amphibole and feldspar, altered with secondary sulfides
AC02	Flow foliated, color layered, porphyritic, primary feldspar?, altered with sulfides
AC03	Fine-grained, miarolitic cavities, altered
AC04	Porphyritic, unaltered, primary hornblende and feldspar
AC05	Porphyritic, unaltered, hornblende and feldspar
60763	Hornblende and feldspar, unaltered
60783	Altered, silicified with sulfides
60783	Altered, silicified with sulfides
PI01	Altered, silicified with sulfides, pseudomorphs of feldspar
LU01	Porphyritic with hornblende and plagioclase, minor alteration
LU02	Porphyritic with hornblende and plagioclase, unaltered, darker color than LU01, 03, 04, 05
LU03	Porphyritic with hornblende and plagioclase, unaltered
LU04	Porphyritic with some hornblende and plagioclase, altered
LU05	Porphyritic with hornblende and plagioclase, minor alteration, finer grained than LU04 or 05
LU06	Porphyritic with hornblende and plagioclase, altered
LU07	Porphyritic with hornblende and plagioclase, altered, potassium feldspar?
LU08	Porphyritic with hornblende and plagioclase, altered
LU09	Altered with minor sulfides
LU10	Altered, some primary hornblende

Of the 19 samples collected, seven were selected for $^{40}Ar/^{39}Ar$ age-spectrum analysis of primary and secondary minerals. These samples were selected to cover the aerial outcrop extent of the intrusive body. Primary magmatic hornblende was separated from samples AC04, 60763, LU02, LU06, and LU09; magmatic potassium feldspar was separated from sample 60763 (fig. 3*B*; table 6). Two of these hornblende separates, samples AC04 and LU02, were analyzed in duplicate. White mica (sericite), an alteration phase, was separated from samples AC01 and PI01. Sample AC01 contained two distinct grain sizes of sericite, and these were both concentrated and analyzed. Locations of the samples are shown in figures 4, 5, and 6, and listed in table 3. Detailed sample descriptions are given in appendix 1. Mineral separates were prepared using standard crushing, sieving, gravimetric (heavy liquid), and magnetic separation techniques. Samples were hand-picked to an estimated visual purity of > 99.9 percent.

Mineral separates for $^{40}Ar/^{39}Ar$ dating were loaded in aluminum foil capsules, sealed in silica vials, and irradiated in two separate irradiation packages—one for 20 hours and another for 15 hours—in the central thimble of the U.S. Geological Survey TRIGA reactor in Denver, Colo. (Dalrymple and others, 1981). Vertical and horizontal gradients in neutron fluence in the irradiated packages were monitored by standards distributed along the length of each vial; the geometry of the irradiated packages was such that each unknown sample was adjacent to at least one standard. Neutron fluence was monitored using hornblende standard MMhb-1 (Samson and Alexander, 1987), which has a K-Ar age of 523.1 ± 2.6 Ma (Renne and others, 1998), and sanidine standard FCT, with an internally calibrated age of 28.03 Ma. Corrections for reactor-produced interfering reactions were made using argon isotopes of K_2SO_4 and CaF_2 irradiated in each package.

After irradiation, the samples were progressively degassed in a double-vacuum resistance furnace in a series of 20-minute-long steps to a maximum temperature of 1,450°C. After each heating step, the gas was collected and purified using Zr-Al-Ti getters, and all five argon isotopes (40, 39, 38, 37, and 36) were measured using a Mass Analyser Products mass spectrometer operated in the static mode. Abundances of all argon isotopes were determined using a Faraday cup collector. Apparent ages were calculated using decay constants recommended by Steiger and Jäger (1977). Argon data were evaluated using age spectra, apparent $^{39}Ar/^{37}Ar$ ratios (for whole rock and hornblende

Table 5. Petrography.

[Abbreviations: plag, plagioclase; hbl, hornblende; pyr, pyroxene; py, pyrite; FeO, opaques; sph, sphene; ap, apatite; Ks, potassium feldspar; qtz, quartz; pseudo, pseudomorph; gr, green; oxy, oxyhornblende rims; alt, altered; ser, sericite; carb, carbonate; zeo, zeolite; leuco, leucoxene; chl, chlorite]

Sample no.	Phenocrysts							
	plag	hbl	pyr	FeO	sph	ap	Ks	qtz
AC01	Pseudo	Pseudo	Pseudo	Minor	Minor			
AC02	Slightly altered		Pseudo	Pseudo	Minor	Minor	Minor	
AC03	Pseudo	Pseudo	Pseudo	Abundant				
AC04	Oligoclase	Gr w/ oxy	Minor	Abundant	Minor	Minor		
AC05	Oligoclase	Gr w/ oxy	Minor	Abundant	Minor	Minor		
60763	Oligoclase/andesine	Gr w/ oxy	Minor	Minor	Minor	Minor	Minor	
60783	Oligoclase	Pseudo	Pseudo	Minor	Minor	Minor	Pseudo	Minor
60783A	Andesine	Pseudo	Pseudo	Minor	Minor	Minor	Minor	
PI01	Altered	Pseudo	Minor	Minor	Minor	Minor	Minor	
LU01	Slightly altered	Partial alt	?					
LU02	Oligoclase	Green	Abundant	Minor	Minor	Minor		
LU03	Oligoclase	Oxyhbl	Abundant	Minor	Minor	Minor		
LU04	Slightly altered	Pseudo	Pseudo	Minor	Minor			
LU05	Oligoclase/andesine	Gr w/ oxy	Augite	Minor	Minor	Minor	Minor	
LU06	Slightly altered	Pseudo	Pseudo	Minor	Minor			
LU07	Altered	Pseudo	Minor	Minor	Minor			
LU08	Oligoclase	Green	Abundant	Minor	Minor	Minor		
LU09	Altered	Pseudo						
LU10	Slightly altered	Pseudo	Minor					

samples), and $^{40}Ar/^{36}Ar$ versus $^{39}Ar/^{36}Ar$ isochron diagrams (York, 1969). The determination of whether the individual apparent ages in an age spectrum yielded a "plateau" was made using the criteria of Fleck and others (1977). Following these criteria, a plateau is defined as comprising two or more contiguous gas fractions, which yield apparent ages that are statistically indistinguishable at the 95 percent confidence level (using the critical value test of McIntyre, 1963, as applied by Dalrymple and Lanphere, 1969) and which together constitute greater than 50 percent of the total potassium-derived ^{39}Ar ($^{39}Ar_K$) released in the incremental heating experiment. Plateau ages were calculated using a weighted mean based on the proportion of $^{39}Ar_K$ released during the incremental heating experiment. Plateau ages are given at $\pm 1\sigma$ and include the analytical uncertainty in the determination of the fluence parameter *J*. A summary of the results of the $^{40}Ar/^{39}Ar$ incremental heating experiments are listed in table 7 along with our preferred ages based on interpretation of the isotopic analyses. Individual age spectra are shown in figures 7 through 17. Detailed $^{40}Ar/^{39}Ar$ analytical data for individual samples are listed in table 6. Complete details on procedures used in the U.S. Geological Survey, Denver Argon Geochronology Laboratory are presented in Snee (2002).

Data

Magmatic hornblende from unaltered or slightly altered samples AC04, LU02, and LU06 were the first samples to be irradiated for this study. Hornblende samples AC04, 60763, LU02, and LU09 were irradiated in a subsequent irradiation package. Argon age-spectrum analyses of these samples resulted in simple plateaus with three statistically unique age groups of 12.7±0.1 Ma (error quoted at 1σ; 1 sample), 11.93±0.07 Ma (1 sample and its replicate), and 11.68±0.04 Ma (3 samples plus 1 replicate; tables 4 and 5). Magmatic potassium feldspar, separated from sample 60763 and irradiated in the second irradiation package, yielded an argon age spectrum that increases in age from a lower temperature age of 11.5 Ma to a higher temperature age of 12.6 Ma (tables 6 and 7). Two alteration sericites, one finer grained and one coarser grained, were separated from sample AC01 and irradiated in the second irradiation package; both of these yielded simple plateaus with statistically identical apparent ages of 11.0±0.2 Ma. A small amount of alteration sericite separated from sample PI01 yielded a disturbed spectrum with the majority of the argon resulting in an apparent age of 12.5±0.2 Ma—significantly different in age from sericite sample AC01 (tables 6 and 7).

Table 5. Petrography—*Continued.*

Sample no.	Groundmass	Alteration	Photos
AC01	Pilotaxitic plag microlites	Altered: ser, py, leuco, carb, chl, FeO	1, 2, 3, 4, 5
AC02	Felted quartzofeldspathic	Altered: ser, py, carb, chl, carb veinlets	6, 7, 8, 9, 10, 11
AC03	Altered + vugs	Altered: ser, carb, chl, qtz, FeO	12, 13, 14
AC04	Felted quartzofeldspathic	Unaltered	15, 16
AC05	Felted quartzofeldspathic	Unaltered	17, 18, 19
60763	Felted quartzofeldspathic w/ pyr and vugs	Unaltered	48, 49
60783	Altered plag w/ ser and carb	Altered: ser, py, carb, FeO, chl	39, 40, 41, 42, 43
60783A	Felted quartzofeldspathic	Altered: ser, py, carb, FeO, chl, qtz	44, 45, 46, 47
PI01	Recystallized(?) w/ Ks, qtz, carb	Altered: ser, carb, chl, qtz, FeO	50, 51, 52, 53, 54
LU01	Pilotaxitic plag microlites + vugs w/ zeo	Mod altered: ser, py, carb, chl, FeO	20, 21
LU02	Randomly oriented plag microlites w/ pyr	Unaltered: carb veinlet	22, 23
LU03	Felted quartzofeldspathic	Unaltered	24, 25, 26, 27, 28, 29
LU04	Felted quartzofeldspathic	Altered: chl, carb, FeO, carb veinlets	30, 31
LU05	Felted quartzofeldspathic w/ carb	Unaltered	32, 33
LU06	Felted quartzofeldspathic	Altered: chl, carb, FeO	34, 35
LU07	Felted quartzofeldspathic w/ carb	Altered: chl, carb, FeO, ser	No photograph
LU08	Pilotaxitic plag microlites	Unaltered	36
LU09	Altered to py, carb	Altered: py, chl, carb, FeO	No photograph
LU10	Felted quartzofeldspathic w/ carb	Altered: py, chl, carb, FeO, ser	37, 38

Interpretation

The $^{40}Ar/^{39}Ar$ apparent ages derived from the age-spectrum analyses for each mineral in this study mark the time when each mineral closed to diffusion of argon. Closure to diffusion is controlled chiefly by temperature but also by cooling rate (Carslaw and Jaeger, 1959; Dodson, 1973), chemical compositional variation (for example, Till and Snee, 1995), and structural state variation or strain history (Cosca and others, 1992). The closure-temperature is higher for fast cooling, and conversely, is lower if cooling was slow. Commonly accepted closure temperatures that span a range from rapid (1,000°C/m.y.) to slow cooling (5°C/m.y.) are 580°–480°C for hornblende (Harrison, 1981) and 325°–270°C for muscovite (Snee and others, 1988; $2M_1$ structural state). If a mineral forms under temperature conditions above its argon closure temperature, there will be a time period of cooling during which argon freely moves in and out of the mineral and closure is not realized. In contrast, if a mineral forms under temperature conditions below its closure temperature, the argon system of the mineral closes immediately, and the apparent age of the mineral marks the time of its formation without any period of cooling. The geologic environment of the Balsapuerto area can be used to constrain the interpretation of the apparent ages for the samples in this study.

Petrographic examination of the samples used in this study for argon geochronology indicates that all 19 samples are unaltered to altered, porphyritic, subvolcanic igneous rocks with a composition ranging from andesite to dacite. The porphyritic texture and presence of miarolitic cavities requires a relatively shallow emplacement level. Many of the samples were hydrothermally altered indicating the presence of heat and fluids after their original formation.

Hornblende $^{40}Ar/^{39}Ar$ plateau dates form three age groups of approximately 12.7, 11.9, and 11.7 Ma. These dates are the time when each of these samples cooled through an argon closure temperature of ~580°C—a closure temperature consistent with the mode of emplacement of these rocks. The age differences of these three groups can be interpreted in three ways. First, magma was emplaced at least three times during the history of the intrusive body. Second, the intrusive body is 12.7 Ma or older, and the three dates indicate the time of closure to diffusion of argon. A third possible explanation for the three age groups is that there were two or three events that reset the argon system. This third interpretation is unacceptable because no evidence for reheating to greater than 580°C is

Table 6. $^{40}Ar/^{39}Ar$ analytical data for individual samples

Temp°C	$^{40}Ar_R$	$^{39}A_{rK}$	$^{40}Ar_R/^{39}Ar_K$	$^{39}Ar_K/^{37}Ar_{Ca}$	Radiogenic yield (%)	$\%39Ar_K$ total	Apparent age & error (Ma at 1 sigma)
AC01/3/DD83—White mica (Total-gas date: 10.91+/-.13 Ma; Plateau date: 10.96+/-0.1 Ma;, J= .003624 +/- 0.1 %; wt. 54.2 mg)							
550	0.04301	0.02762	1.557	94.15	14.1	1.5	10.15 +/- 1.08
650	0.09426	0.06149	1.533	80.86	55.9	3.3	9.99 +/- .43
750	0.0386	0.02747	1.405	66.37	63.2	1.5	9.16 +/- .44
850	1.34578	0.80044	1.681	124.42	90.1	43.2	10.96 +/- .02
900	0.27558	0.16274	1.693	203.08	91.5	8.8	11.04 +/- .13
950	0.30365	0.18058	1.682	191.61	90.3	9.7	10.96 +/- .07
1000	0.25533	0.15182	1.682	186.18	86.2	8.2	10.96 +/- .21
1050	0.24817	0.14615	1.698	162.15	81.1	7.9	11.07 +/- .12
1100	0.23616	0.13935	1.695	88.69	76.5	7.5	11.05 +/- .16
1150	0.14725	0.08771	1.679	35.35	69.2	4.7	10.94 +/- .10
1250	0.09626	0.0572	1.683	14.9	45.2	3.1	10.97 +/- .32
1450	0.0193	0.01138	1.697	19.03	28.8	0.6	11.06 +/- 1.58
AC01/58/DD83—Fine white mica (Total-gas date: 11.11+/-.60 Ma; Plateau date: 11.1+/-0.4 Ma; J= .003778 +/- 0.1 %; wt. 21.5 mg)							
550	0.01424	0.00902	1.579	0.87	7.8	2.4	10.73 +/- 3.77
650	0.06191	0.04102	1.509	0.64	54.1	11.1	10.26 +/- .12
750	0.10631	0.06612	1.608	0.26	54	17.8	10.92 +/- .48
850	0.11617	0.07155	1.624	0.08	35	19.3	11.03 +/- .25
900	0.06689	0.04072	1.643	3.2	56.6	11	11.16 +/- 1.17
950	0.03088	0.01894	1.63	6.25	21.9	5.1	11.08 +/- 1.20
1050	0.11204	0.06807	1.646	5.79	58.2	18.4	11.18 +/- .37
1150	0.05844	0.03504	1.668	7.4	48.7	9.4	11.33 +/- .16
1250	0.02858	0.01516	1.885	2.9	37.3	4.1	12.80 +/- 1.37
1400	0.01124	0.00525	2.14	1.88	25.8	1.4	14.53 +/- 3.45
AC04/71/DD82—Hornblende (Total-gas date: 11.89+/-.18 Ma; Plateau date: 11.94+/-0.07 Ma; J= .004924 +/- 0.1 %; wt. 175.9 mg)							
700	0.00912	0.00972	0.938	1.4	2.1	0.4	8.31 +/- 4.14
850	0.02134	0.01771	1.205	1.27	17.6	0.8	10.67 +/- .74
1000	0.00724	0.00666	1.086	0.53	12.5	0.3	9.62 +/- 5.42
1050	0.22542	0.16615	1.357	0.33	77.6	7.2	12.01 +/- .16
1100	0.55702	0.41386	1.346	0.33	89.3	18	11.92 +/- .10
1150	1.32551	0.98188	1.35	0.33	89.4	42.8	11.95 +/- .04
1200	0.65991	0.48874	1.35	0.32	88.3	21.3	11.95 +/- .02
1250	0.26905	0.19999	1.345	0.24	83.9	8.7	11.91 +/- .13
1300	0.00684	0.00845	0.81	0.05	23.5	0.4	7.18 +/- 4.94
1350	0.00041	0.00131	0.314	0.06	2.7	0.1	2.79 +/- 17.13

Table 6. $^{40}Ar/^{39}Ar$ analytical data for individual samples—*Continued.*

Temp°C	$^{40}Ar_R$	$^{39}A_{rK}$	$^{40}Ar_R/^{39}Ar_K$	$^{39}Ar_K/^{37}Ar_{Ca}$	Radiogenic yield (%)	%$39Ar_K$ total	Apparent age & error (Ma at 1 sigma)
AC04/5/DD83—Hornblende (Total-gas date: 11.90+/-.14 Ma; Plateau date: 11.93+/-0.07 Ma; J= .0037265 +/- 0.1 %; wt. 268.8 mg)							
700	0.00977	0.00696	1.404	1.23	4.7	0.3	9.41 +/- 3.03
800	0.0081	0.00559	1.449	3.93	24.5	0.3	9.72 +/- 5.10
900	0.02891	0.0185	1.563	4.39	39	0.9	10.48 +/- .98
1000	0.00871	0.00553	1.575	0.82	24.6	0.3	10.56 +/- 6.28
1050	0.04258	0.02424	1.756	0.34	29	1.1	11.77 +/- .93
1100	0.62171	0.35044	1.774	0.33	90.2	16.2	11.89 +/- .05
1125	0.42954	0.24187	1.776	0.33	91.8	11.2	11.90 +/- .15
1150	0.68277	0.38456	1.775	0.33	91.2	17.8	11.90 +/- .02
1200	0.48147	0.27021	1.782	0.32	88.8	12.5	11.94 +/- .10
1250	0.34137	0.19021	1.795	0.19	85.9	8.8	12.02 +/- .12
1300	0.08644	0.04788	1.805	0.05	72.5	2.2	12.10 +/- .35
1450	1.08874	0.61084	1.782	0.32	91.3	28.3	11.94 +/- .06
60763/2/DD83—K-feldspar (Total-gas date: 12.21+/-.20 Ma; Cooling profile: 12.62+/-0.04 Ma, 11.51 +/- 0.8; J= .003698 +/- 0.1 %; wt. 45 mg)							
500	0.00134	0.00012	11.101	3.99	3.9	0	72.58 +/- 22.21
600	0.0286	0.01149	2.489	9.18	9.2	0.5	16.53 +/- .42
650	0.05046	0.02725	1.851	12.78	38.5	1.3	12.31 +/- .77
700	0.09185	0.05314	1.728	11.1	56	2.5	11.49 +/- .38
750	0.08246	0.04833	1.706	5.59	60.9	2.2	11.35 +/- 1.47
800	0.18999	0.10955	1.734	5.69	60.4	5.1	11.53 +/- .52
850	0.16264	0.09345	1.74	7.98	73.6	4.3	11.57 +/- .68
900	0.16462	0.09431	1.745	8.25	77.6	4.4	11.61 +/- .49
950	0.15993	0.08904	1.796	8.04	79.5	4.1	11.94 +/- .36
1000	0.14167	0.07919	1.789	10.57	77.4	3.7	11.90 +/- .29
1050	0.15821	0.08786	1.801	14.48	74.1	4.1	11.97 +/- .28
1150	0.33566	0.18658	1.799	13.16	78.7	8.6	11.96 +/- .07
1250	0.7017	0.38407	1.827	10.68	72	17.7	12.15 +/- .02
1350	1.52486	0.8052	1.894	25.19	72.4	37.2	12.59 +/- .03
1450	0.18178	0.09563	1.901	25.76	63.9	4.4	12.64 +/- .16

Table 6. $^{40}Ar/^{39}Ar$ analytical data for individual samples—*Continued.*

Temp°C	$^{40}Ar_R$	$^{39}A_{rK}$	$^{40}Ar_R/^{39}Ar_K$	$^{39}Ar_K/^{37}Ar_{Ca}$	Radiogenic yield (%)	$\%39Ar_K$ total	Apparent age & error (Ma at 1 sigma)
60763/4/DD83—Hornblende (Total-gas date: 12.81+/-.09 Ma; Plateau age: 12.67+/-0.1 Ma; J= .003769 +/- 0.1 %; wt. 236.9 mg)							
700	0.01987	0.00338	5.88	0.83	7.8	0.1	39.54 +/- 6.52
800	0.01937	0.00905	2.141	1.26	24.2	0.4	14.50 +/- 3.15
900	0.04805	0.0234	2.054	1.79	30.7	1	13.91 +/- .96
1000	0.072	0.03855	1.8687	1.11	44.8	1.6	12.66 +- .18
1050	0.33413	0.17943	1.862	0.34	75.8	7.4	12.62 +/- .23
1100	1.10941	0.59337	1.87	0.35	87.8	24.4	12.67 +/- .04
1150	1.62819	0.8712	1.869	0.34	91.7	35.8	12.66+/-.03
1200	0.75793	0.40452	1.874	0.34	89.7	16.6	12.69+/-.05
1250	0.46634	0.2379	1.96	0.3	85.2	9.8	13.28 +/- .03
1300	0.11627	0.05917	1.965	0.29	79.5	2.4	13.31 +/- .33
1350	0.03044	0.01409	2.16	0.28	38.4	0.6	14.63 +/- 1.32
PI01/1/DD83—White mica (Total-gas date: 12.44+/-.45 Ma; 0ne-step age: 12.5+/-0.2 Ma; J= .003757 +/- 0.1 %; wt. 4.5 mg)							
650	0.03448	0.02348	1.468	93.36	25.7	14.6	9.92 +/- 1.36
1100	0.23025	0.12404	1.856	122.65	59.7	76.9	12.54 +/- .16
1450	0.03227	0.01375	2.347	25.88	42	8.5	15.84 +/- 1.12
LU02/70/DD82—Hornblende (Total-gas date: 11.76+/-.08 Ma; Plateau age: 11.65+/-0.09 Ma; J= .004957 +/- 0.1 %; wt. 247.5 mg)							
700	0.05799	0.01837	3.157	0.12	10.2	0.6	28.01 +/- .70
850	0.02881	0.02315	1.244	0.04	8.6	0.7	11.09 +/- .60
1000	0.04697	0.03442	1.365	0.47	37.6	1	12.16 +/- .52
1050	0.23862	0.18039	1.323	0.39	81.6	5.5	11.79 +/- .10
1100	0.64124	0.49041	1.308	0.39	89.2	14.9	11.66 +/- .04
1125	1.08449	0.82886	1.308	0.38	94.9	25.1	11.66 +/- .02
1150	1.01884	0.78135	1.304	0.38	94.6	23.7	11.62 +/- .02
1200	0.84213	0.64186	1.312	0.37	93.7	19.5	11.69 +/- .07
1250	0.36493	0.27985	1.304	0.18	86.5	8.5	11.62 +/- .31
1400	0.02397	0.01728	1.388	0.01	36.8	0.5	12.37 +/- 1.92

Table 6. $^{40}Ar/^{39}Ar$ analytical data for individual samples—*Continued.*

Temp°C	$^{40}Ar_R$	$^{39}A_{rK}$	$^{40}Ar_R/^{39}Ar_K$	$^{39}Ar_K/^{37}Ar_{Ca}$	Radiogenic yield (%)	$\%39Ar_K$ total	Apparent age & error (Ma at 1 sigma)
LU02/6/DD83—Hornblende (Total-gas date: 11.79+/-0.09 Ma; Plateau age: 11.70+/-0.06 Ma; J= .003646 +/- 0.1 %; wt. 244.6 mg)							
700	0.01901	0.00323	5.882	0.39184	7.4	0.1	38.28 +/- 9.24
800	0.00684	0.00161	4.244	0.51783	35.4	0.1	27.70 +/- 21.25
900	0.01223	0.00532	2.298	0.9525	31.2	0.2	15.05 +/- 5.70
1000	0.02236	0.01014	2.205	0.90307	25.9	0.4	14.45 +/- 3.58
1025	0.02351	0.01151	2.042	0.84542	54.2	0.5	13.38 +/- .58
1050	0.03231	0.0172	1.879	0.48727	64.7	0.7	12.32 +/- .96
1100	0.72784	0.40549	1.795	0.39231	89.6	17	11.77 +/- .02
1125	0.3945	0.22007	1.793	0.388	83.4	9.2	11.75 +/- .12
1150	0.83215	0.46793	1.778	0.38529	94.7	19.6	11.66 +/- .05
1200	1.30285	0.7326	1.778	0.3837	95.2	30.6	11.66 +/- .04
1250	0.39967	0.22282	1.794	0.3176	91.1	9.3	11.76 +/- .08
1400	0.5274	0.2931	1.799	0.23768	89.9	12.3	11.80 +/- .03
LU06/72/DD82—Hornblende (Total-gas date: 11.66+/-.24 Ma; Plateau age: 11.64+/-0.1 Ma;, J= .004989 +/- 0.1 %; wt. 77.8 mg)							
750	0.00232	0.00268	0.865	0.05	0.7	0.2	7.77 +/- 12.84
950	0.01106	0.0069	1.602	0.17	14.8	0.6	14.36 +/- 5.20
1050	0.11864	0.0907	1.308	0.39	69.3	7.6	11.73 +/- 1.17
1150	0.65174	0.50194	1.298	0.38	92.2	41.8	11.65 +/- .04
1225	0.65473	0.50443	1.298	0.37	94.2	42	11.64 +/- .12
1350	0.11999	0.09269	1.295	0.32	78.8	7.7	11.61 +/- .21
1400	0.00103	0.00093	1.112	0.22	5.3	0.1	9.98 +/- 4.33
LU09/59/DD83—Hornblende (Total-gas date: 12.07+/-.19 Ma; Plateau age: 11.72+/-0.08 Ma; J= .003785 +/- 0.1 %; wt. 101.8 mg)							
700	0.0101	0.00222	4.557	0.89	5.8	0.2	30.85 +/- 9.60
900	0.03408	0.01285	2.652	1.16	33.4	1.2	18.02 +/- 1.68
1000	0.04695	0.02285	2.054	1	43.9	2.2	13.97 +/- .53
1050	0.09076	0.05009	1.812	0.43	77.2	4.8	12.33 +/- .37
1100	0.37066	0.21558	1.719	0.39	90.6	20.8	11.70 +/- .11
1150	0.88826	0.51534	1.724	0.38	95.2	49.7	11.73 +/- .05
1200	0.20055	0.11548	1.737	0.36	89.9	11.1	11.82 +/- .24
1250	0.11526	0.06415	1.797	0.19	80.6	6.2	12.23 +/- .56
1300	0.03558	0.01376	2.586	0.08	63.3	1.3	17.57 +/- 1.98
1450	0.04784	0.02482	1.927	0.15	62.8	2.4	13.11 +/- .65

Table 7. Interpreted $^{40}Ar/^{39}Ar$ age-spectrum dates, Balsa prospect, Peru.

[K spar, potassium feldspar]

Sample no.	Material dated	Preferred age (Ma)	Comments
AC01	Alteration sericite 1	10.96+0.1	Plateau; 94% released ^{39}Ar
	Alteration sericite 2	11.1+0.4	Plateau; 80% released ^{39}Ar
AC04	Hornblende	11.94+0.07	Plateau; 98% released ^{39}Ar
	Hornblende replicate	11.93+0.07	Plateau; 98% released ^{39}Ar
60763	Hornblende	12.67+0.1	Plateau; 86% released ^{39}Ar
	Primary magmatic K spar	12.6 to 11.5	Cooling profile
PI01	Alteration sericite	12.5+0.2	Single step; 77% released ^{39}Ar
LU02	Hornblende	11.65+0.09	Plateau; 82% released ^{39}Ar
	Hornblende replicate	11.70+0.06	Plateau; 98% released ^{39}Ar
LU06	Hornblende	11.64+0.1	Plateau; 92% released ^{39}Ar
LU09	Hornblende	11.72+0.08	Plateau; 82% released ^{39}Ar

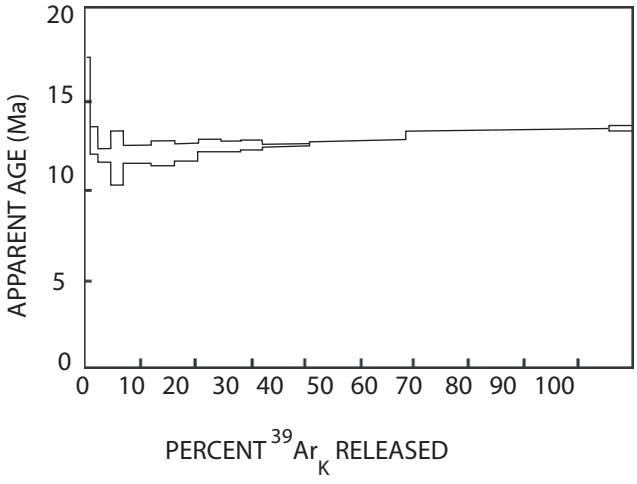

Figure 7. $^{40}Ar/^{39}Ar$ age spectrum for potassium feldspar, sample 60763/2/DD83. This sample yielded a higher temperature age of 12.62±0.04 Ma and a lower temperature age of 11.51±0.08 Ma.

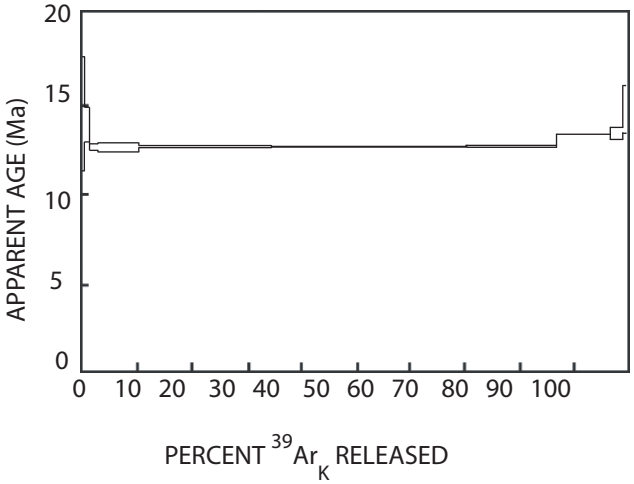

Figure 8. $^{40}Ar/^{39}Ar$ age spectrum for hornblende, sample 60763/4/DD83. The interpreted age of this sample is 12.67±0.10 Ma.

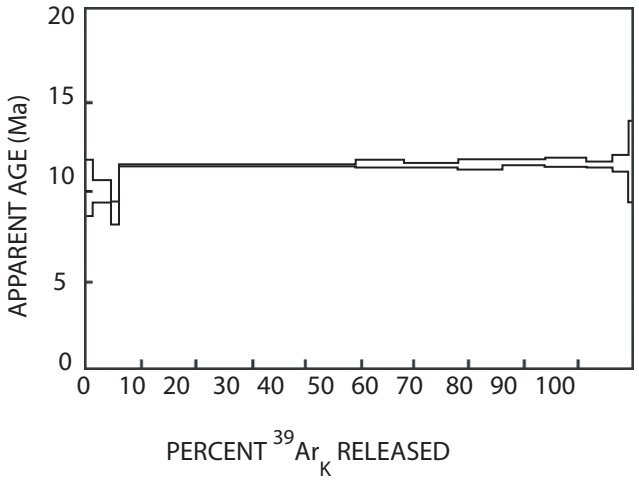

Figure 9. $^{40}Ar/^{39}Ar$ age spectrum for sericite concentrate, sample AC01/3/DD83. The interpreted age of this sample is 11.1±0.04 Ma.

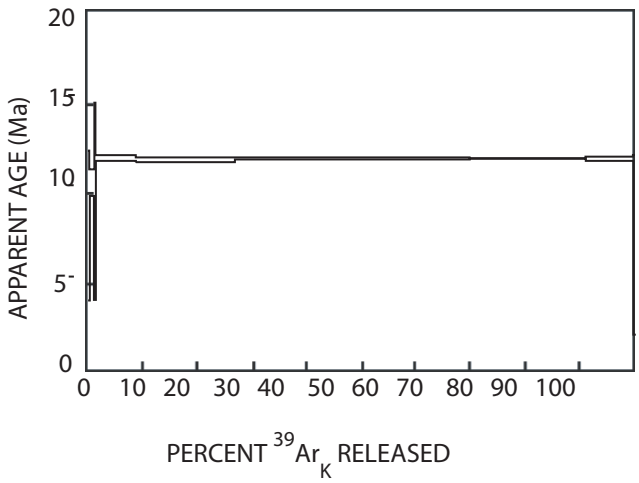

Figure 12. $^{40}Ar/^{39}Ar$ age spectrum for hornblende, sample AC04/71/DD82. The interpreted age of this sample is 11.92±0.07 Ma.

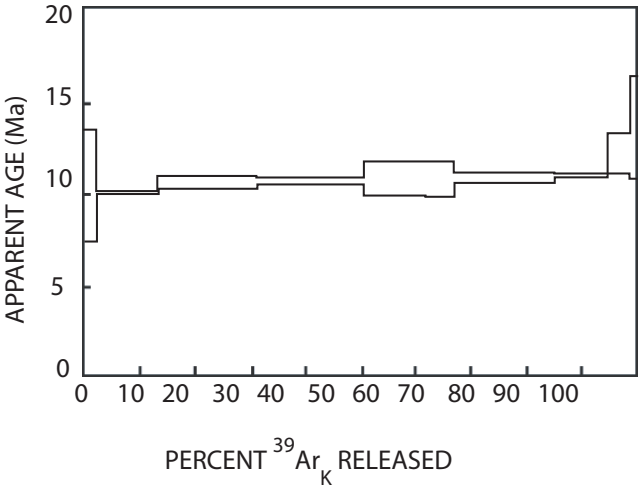

Figure 10. $^{40}Ar/^{39}Ar$ age spectrum for sericite, sample AC01/58/DD83. The interpreted age of this sample is 10.96±0.10 Ma.

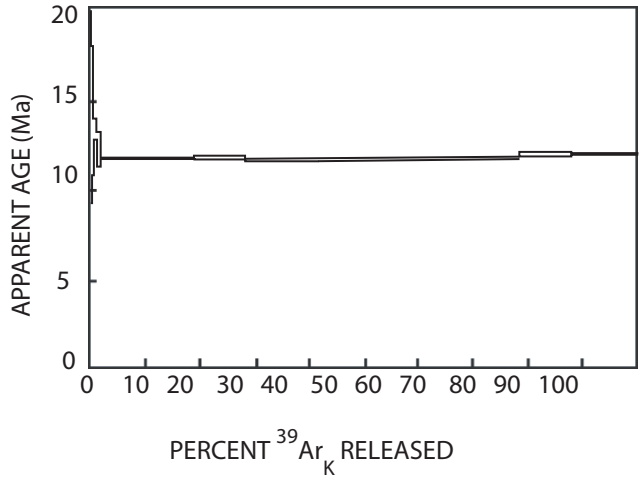

Figure 13. $^{40}Ar/^{39}Ar$ age spectrum for hornblende, sample LU02/6/DD83. The interpreted age of this sample is 11.70±0.06 Ma.

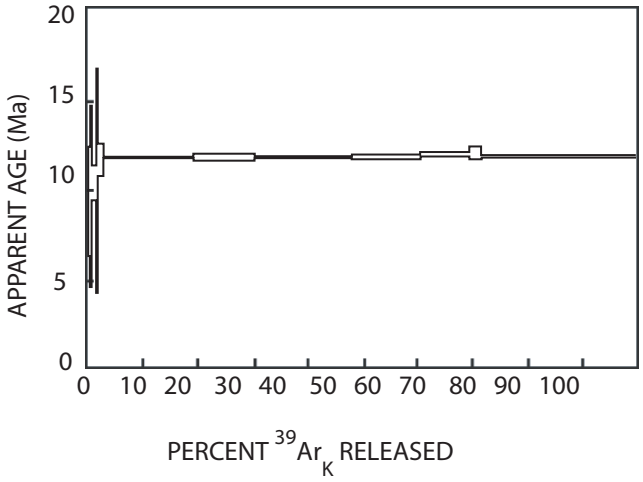

Figure 11. $^{40}Ar/^{39}Ar$ age spectrum for hornblende, sample AC04/5/DD83. The interpreted age of this sample is 11.93±0.07 Ma.

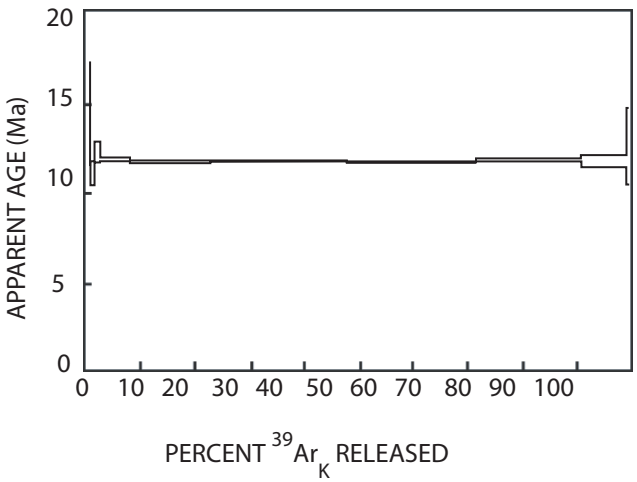

Figure 14. $^{40}Ar/^{39}Ar$ age spectrum for hornblende, sample LU02/70/DD82. The interpreted age of this sample is 11.65±0.09 Ma.

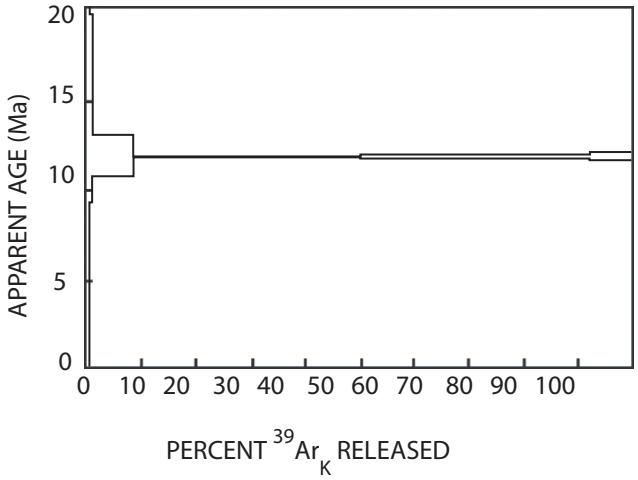

Figure 15. $^{40}Ar/^{39}Ar$ age spectrum for hornblende, sample LU06/72/DD82. The interpreted age of this sample is 11.64±0.1 Ma.

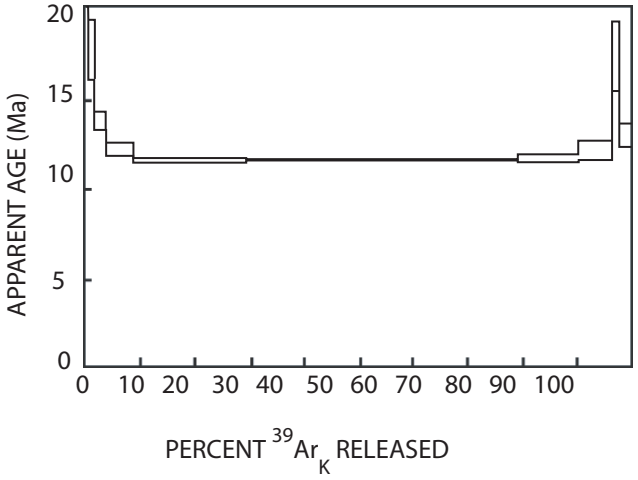

Figure 16. $^{40}Ar/^{39}Ar$ age spectrum for hornblende, sample LU09/59/DD83. The interpreted age of this sample is 11.72±0.08 Ma.

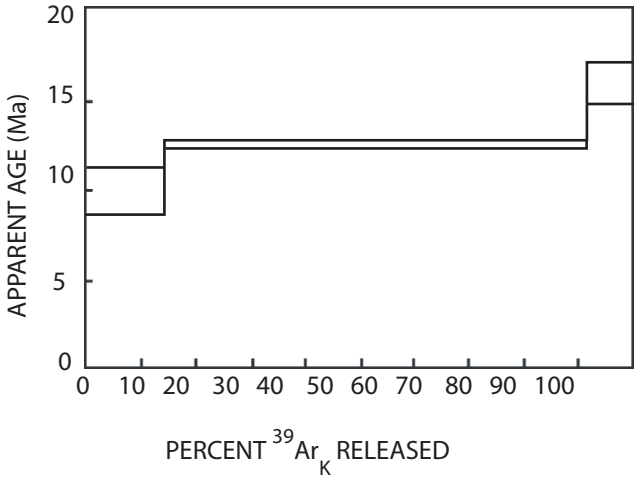

Figure 17. $^{40}Ar/^{39}Ar$ age spectrum for sericite, sample PI01/1/DD83. The interpreted age of this sample is 12.5±0.2 Ma.

petrographically exhibited by the samples, and the age spectra of older hornblende samples do not show evidence for resetting of the argon systems. Magmatic potassium feldspar from one of the oldest of these samples (60763) shows a typical age spectrum for apparent multi-domain argon closure as has been well documented by many investigators (for example, Lovera and others, 1993; Harrison and others, 1991; Lovera and others, 1991). In this model for argon diffusion in potassium feldspar, argon is released from the feldspar during heating in the experimental furnace. The argon release from several diffusion domains with unique closure temperatures ranging from ≥350° to ≤150°C, controls the character of the age spectrum. A gradual increase in apparent ages from lower ages at lower extraction temperatures to higher ages at higher extraction temperatures reflects this mixing; the resultant age spectrum is a virtual cooling profile for the feldspar sample. The age range of 12.6 to 11.5 Ma can be interpreted to reflect the time of cooling of this potassium feldspar from ≥350° to ≤150°C; this indicates that the magma in this location cooled rapidly from hornblende argon closure temperature of ~580°C through ≤150°C, a rate of nearly 400°C/m.y. during ~1.1 m.y. In the area of sample 60763, the intrusive body was at a much lower temperature than that of argon closure in hornblende at the time of closure of younger hornblende samples at 11.9 and 11.7 Ma. This suggests multiple periods of emplacement of relatively small volumes of magma but does not exclude the other alternative.

Many of the samples in this study exhibit petrographic evidence for a later period(s) of hydrothermal alteration. Sericite apparent ages can be interpreted in a manner similar to that for the interpretation of the hornblende ages. The temperature of formation of the most altered rocks, which exhibit sericite alteration, is about 350°C; this temperature is essentially the argon closure temperature of muscovite (Snee and others, 1988). The sericite dates suggest two periods of alteration, one at 12.5 Ma and the other at 11.0 Ma, although the age spectrum for the older sample is slightly disturbed and should be interpreted with caution. If two periods of hydrothermal activity did occur, this would indicate that the magmatic/hydrothermal system was active from ≥12.7 to ≤11.0 Ma. This is also consistent with the interpretation that several periods of magmatic activity with resultant heat and fluid flow occurred between ~12.7 and ~11.0 Ma.

Discussion

Emplacement of the intrusive body(ies) in the Balsapuerto Dome began at about 12.7 Ma, and activity continued until about 11 Ma. The age ranges determined by Ar/Ar geochronology on hornblende and potassium feldspar indicate multiple periods of emplacement of relatively small volumes of magma between 12.7 and 11.6 Ma, but does not exclude a period of thermal activity and high-temperature cooling throughout this age range. Many samples show evidence of secondary hydrothermal alteration. The white mica ages determined by Ar/Ar geochronology indicate that at least

two periods of hydrothermal activity occurred at 12.5 and 11.0 Ma, throughout the period of emplacement and cooling of the intrusive body below about 150°C. If two periods of hydrothermal activity did occur, this would indicate that the magmatic/hydrothermal system was active from ≥12.7 to ≤11.0 Ma. This is also consistent with the interpretation that several periods of magmatic activity with resultant heat and fluid flow occurred between ~12.7 and ~11.0 Ma. Geochemical analyses of selected samples will provide information about the magma source(s). Knowledge of the magma source may help to resolve whether there were multiple periods of intrusion or one episode of intrusion and a prolonged cooling event; it may also provide information about the angle of the subducting slab and the extent of subduction of the Carnegie Ridge and underthrusting by the Brazil Shield.

The ages of the hypabyssal rocks in central and northern Peru have been used to constrain the age of the sub-Andean deformation, because the intrusions occurred after the deformation had ceased. Prior to this work, isotopic ages were only determined for the Pucallpa samples. As a result of the 5–4.5 Ma (Stewart, 1971) age determination for the Pucallpa samples, the sub-Andean deformation was assumed to have occurred between 10 and 8 Ma (Benavides-Cáceres, 1999). This interpretation may need to be revised. The 5–4.5 Ma age determined for the Pucallpa samples is likely an approximate age because of the possibility of argon loss from cryptoperthite. Our analyses show the Balsapuerto igneous rocks to be 12 to 10 Ma. If the hypabyssal rocks in central and northern Peru are synchronous, and the Balsapuerto samples are 12–10 Ma and not 5–4.5 Ma, then the age of deformation may also be older than previously assumed.

The Balsapuerto Dome is probably not a viable source of petroleum. The emplacement of the igneous rocks in the dome postdates the sub-Andean deformation. The magmatic and hydrothermal systems were active after the intrusion, with temperatures not reaching 150°C until about 1 million years after emplacement. The thermal effects associated with emplacement of the intrusion and the associated hydrothermal system are assumed to have been high enough to destroy any petroleum in the host and source rocks.

Summary

Petrographic and $^{40}Ar/^{39}Ar$ age-spectrum dating indicate that andesitic to dacitic magmas were emplaced at relatively shallow crustal levels in the Balsapuerto area, eastern Peru. The doming of the host rocks caused by emplacement of the intrusions occurred after major regional deformation had ceased. These magmas were emplaced from approximately 12.7 to 11.7 Ma. Either several periods of emplacement occurred during this time, or several of the samples record a period of 1 m.y. after emplacement before cooling below the hornblende argon closure temperature of ~580°C. The argon-age spectrum of potassium feldspar co-existing with the oldest hornblende indicates rapid cooling during 1.2 m.y. to below 150°C, yielding a cooling rate of ~400°C/m.y. Hydrothermal alteration has affected more than half of the samples and records the addition of, at a minimum, potassium, silica, sulfur, and carbonate to the rocks. Sericite formed during the alteration yielded apparent ages of 12.5 and 11.0 Ma indicating that alteration occurred during and after emplacement of the magma. The temperatures associated with the long-lived magmatic and hydrothermal system are presumed to have destroyed any petroleum in the system, making the Balsapuerto Dome an unsuitable source for petroleum.

Further work needs to be done to determine the ages of the hypabyssal igneous rocks in the Andean foreland, both in Peru and other locations. The discovery of the 12–10 Ma ages of the Balsapuerto rocks suggests that other igneous rocks of similar origin may also be older than assumed. These hypabyssal igneous rocks are assumed to be younger than the sub-Andean deformation. If the ages of these rocks are used as part of the evidence to support the 10–8 Ma (Phase II) age for the sub-Andean deformation, then the deformation age and the relation to the igneous activity also must be reconsidered.

References Cited

Benavides-Cáceres, V., 1999, Orogenic evolution of the Peruvian Andes—The Andean cycle, *in* Skinner, B.J., ed., Geology and ore deposits of the central Andes: Society of Economic Geologists Special Publication 7, p. 61–107.

Bourden, E., Eissen, J-P., Gutscher, M-A., Monzier, M., Hall, M.L., and Cotton, J., 2003, Magmatic response to early aseismic ridge subduction; the Ecuadorian margin case (South America): Earth and Planetary Science Letters, v. 205, no. 3–4, p. 123–138.

Carslaw, H.S., and Jaeger, J.C., 1959, Conduction of heat in solids: Oxford, Clarendon Press, 510 p.

Cosca, M.A., Hunziker, J.C., Huon, S., and Massone, H., 1992, Radiometric age constraints on mineral growth, metamorphism, and tectonism of the Gummfluh Klippe, Brianconnais domain of the Prealps, Switzerland: Contributions to Mineralogy and Petrology, v. 112, p. 439–449.

Dalrymple, G.B., Alexander, E.C., Lanphere, M.A., and Kraker, G.P., 1981, Irradiation of samples for $^{40}Ar/^{39}Ar$ dating using the Geological Survey TRIGA reactor: U.S. Geological Survey Professional Paper 1176, 55 p.

Dalrymple, G.B., and Lanphere, M.A., 1969, Potassium-argon dating—Principles, techniques, and applications to geochronology: San Francisco, W.H. Freeman and Company, 258 p.

Dodson, M.H., 1973, Closure temperature in cooling geochronological and petrological systems: Contributions to Mineralogy and Petrology, v. 40, p. 259–274.

Dunbar, R.B., Marty, R.C., and Baker, P.A. 1990, Cenozoic marine sedimentation in the Sechura and Pisco Basins, Peru: Palaeogeography, Palaeoclimatology, Palaeoecology, v. 77, no. 3–4, p. 235–261.

Fleck, R.J., Sutter, J.F., and Elliot, D.H., 1977, Interpretation of discordant $^{40}Ar/^{39}Ar$ age spectra of Mesozoic tholeiites from Antarctica: Geochimica et Cosmochimica Acta, v. 41, p. 15–32.

Harrison, T.M., 1981, Diffusion of ^{40}Ar in hornblende: Contributions to Mineralogy and Petrology, v. 78, p. 324–331.

Harrison, T.M., Lovera, O.M., and Heizler, M.T., 1991, $^{40}Ar/^{39}Ar$ results for alkali feldspars containing diffusion domains with differing activation energy: Geochimica et Cosmochimica Acta, v. 55, p. 1,435–1,448.

Jaillard, E., Hérail, G., Monfret, T., Díaz-Martínez, E., Baby, P., Lavenu, A., and Dumont, J.F., 2000, Tectonic evolution of the Andes of Ecuador, Peru, Bolivia, and northernmost Chile, *in* Cordani, U.G., Milani, E.J., Thomaz Filho, A., and Campos, D.A., eds., Tectonic evolution of South America: International Geological Congress, 31st, Rio de Janeiro, p. 481–559.

James, D.E., and Sacks, I.S., 1999, Cenozoic formation of the central Andes—A geophysical perspective, *in* Skinner, B.J., ed., Geology and ore deposits of the central Andes: Society of Economic Geologists Special Publication 7, p. 1–25.

Jordan, T.E., Isacks, B.L., Allmendinger, R.W., Brewer, J.A., Ramos, V.A., and Ando, C.J., 1983, Andean tectonics related to the geometry of the subducted Nazca plate: Geological Society of America Bulletin, v. 94, p. 341–361.

Kley, J., Monaldi, C.R., and Salfity, J.A., 1999, Along-strike segmentation of the Andean foreland—causes and consequences: Tectonophysics, v. 301, p. 75–94.

Lovera, O.M., Heizler, M.T., and Harrison, T.M., 1993, Argon diffusion domains in K-feldspar II—Kinetic properties of MH-10: Contributions to Mineralogy and Petrology, v. 113, p. 381–393.

Lovera, O.M., Richter, F.M., and Harrison,T.M., 1991, Diffusion domains determined by ^{39}Ar release during step heating: Journal of Geophysical Research, v. 96, p. 2,057–2,069.

Mathalone, J.M.P., and Montoya R. M., 1995, Petroleum geology of the sub-Andean basins of Peru, *in* Tankard, A.J., Suarez S. R., and Welsink, H.J., eds., Petroleum basins of South America: American Association of Petroleum Geologists Memoir 62, p. 423–444.

McIntyre, D.B., 1963, Precision and resolution in geochronometry, *in* Albritton, C.C., ed., The fabric of geology: Reading, Mass., Addison-Wesley, p. 112–134.

Mégard, F., 1989, The evolution of the Pacific Ocean margin in South American north of Arica Elbow (18°), *in* Ben-Avraham, Z., ed., The evolution of the Pacific Ocean margins: Oxford Monographs on Geology and Geophysics 8, p. 208–230.

Pichler, H., Hoermann, P.K., and Braun, A.F., 1976, First petrologic data on lavas of the volcano El Reventador (eastern Ecuador): Muenstersche Forschungen zur Geologie und Palaeontologie, no. 38–39, p. 129–141.

Ramos, V.A., and Aleman, A., 2000, Tectonic evolution of the Andes, *in* Cordani, U.G., Milani, E.J., Thomaz Filho, A., and Campos, D.A., eds., Tectonic evolution of South America: International Geological Congress, 31st, Rio de Janeiro, p. 635–685.

Renne, P.R., Swisher, C.C., Deino, A.L., Karner, D.B., Owens, T.L., and DePaolo, D.J., 1998, Intercalibration of standards, absolute ages and uncertainties in $^{40}Ar/^{39}Ar$ dating: Chemical Geology, v. 145, p. 117–152.

Samson, S.D., and Alexander, E.C., 1987, Calibration of interlaboratory $^{40}Ar/^{39}Ar$ dating standard, MMhb-1: Isotope Geoscience, v. 66, p. 27–34.

Sandeman, H.A, Clark, A.H., and Farrar, E., 1997, Lithostratigraphy, petrology and ^{40}Ar-^{39}Ar geochronology of the Crucero Supergroup, Puno Department, SE Peru: Journal of South American Earth Sciences, v. 10, no. 3–4, p. 223–245.

Sébrier, M., and Soler, P., 1991, Tectonics and magmatism in the Peruvian Andes from late Oligocene time to the present, *in* Harmon, R.S., and Rapela, C.W., eds., Andean magmatism and its tectonic setting: Geological Society of America Special Paper 265, p. 259–278.

Snee, L.W., 2002, Argon thermochronology of mineral deposits—A review of analytical methods, formulations, and selected applications: U.S. Geological Survey Bulletin 2194, 39 p. [http://pubs.usgs.gov/bul/b2194].

Snee, L.W., Sutter, J.F., and Kelly, W.C., 1988, Thermochronology of economic mineral deposits—Dating the stages of mineralization at Panasqueira, Portugal, by high-precision $^{40}Ar/^{39}Ar$ age-spectrum techniques on muscovite: Economic Geology, v. 83, p. 335–354.

Soler, P., and Bonhomme, M.G., 1988, New K-Ar age determinations of intrusive rocks from the Cordillera Occidental and Altiplano of central Peru; identification of magmatic pulses and episodes of mineralization: Journal of South American Earth Sciences, v. 1, no. 2, p. 169–177.

Steiger, R.H., and Jäger, E., 1977, Subcommission on geochronology—Convention on the use of decay constants in geo- and cosmochronology: Earth and Planetary Science Letters, v. 36, p. 359–362.

Stewart, J.W., 1971, Neogene peralkaline igneous activity in eastern Peru: Geological Society of America Bulletin, v. 82, p. 2,307–2,312.

Talenti, R.B., 1994, A petrologic transect of the Ecuadorian Andes: Moscow, University of Idaho, M.S. thesis, 111 p.

Till, A.B., and Snee, L.W., 1995, $^{40}Ar/^{39}Ar$ evidence that formation of blueschists in continental crust was synchronous with foreland fold and thrust belt deformation, western Brooks Range, Alaska: Journal of Metamorphic Geology, v. 13, p. 41–60.

Wine, G., Martínez, E., Fernández, J., Caldéron, Y., and Galdós, C., 2003, Significant reserves may remain in parts of Peru's Marañon Basin: Oil and Gas Journal, v. 101, no. 23, p. 32–41.

York, D., 1969, Least squares fitting of a straight line with correlated errors: Earth and Planetary Science Letters, v. 5, p. 320–344.

Appendix 1. Sample Descriptions

Sample AC01

Light gray-green, altered, porphyritic andesite to dacite. Pseudomorphs of large (to as much as 1 cm) euhedral plagioclase phenocrysts in weakly developed planar alignment. Smaller size (to as much as 4 mm) pseudomorphs are formed after hornblende and pyroxene(?) phenocrysts. A few percent of euhedral or fragmental quartz, sphene, and apatite phenocrysts range in size to as much as 2 mm. Groundmass is slightly altered pilotaxitic feldspar microlites. Originally 50 percent of rock was phenocrysts and 50 percent was groundmass. Rock is pervasively altered to sericite, pyrite, leucoxene, carbonate, and chlorite. Phenocrysts are more strongly altered than groundmass, but pyrite is disseminated throughout groundmass. Seventy-five percent of the plagioclase phenocrysts are altered to sericite. Hornblende phenocrysts are pseudomorphs consisting of carbonate, chlorite, pyrite, and sericite. A few pockets or vugs are filled with sericite and carbonate.

Photographs:

1. 4.0-mm across; plane-polarized light. Pseudomorphs of hornblende and plagioclase phenocrysts now altered to sericite, pyrite, chlorite, and carbonate in groundmass of slightly oriented plagioclase microlites.
2. 4.0-mm across; plane-polarized light. Altered plagioclase phenocryst next to a cavity filled with carbonate, sericite, and quartz.
3. 1.0-mm across; plane-polarized light. Plagioclase lath is slightly altered to sericite next to a hornblende pseudomorph of chlorite, carbonate, and pyrite.
4. Same as photograph 3 under crossed-polarized light.
5. 4.0-mm across; plane-polarized light. Phenocryst of quartz and altered plagioclase and pseudomorphs of hornblende in groundmass of plagioclase microlites.

Sample AC02

Medium gray-green, altered, porphyritic andesite to dacite. Very similar in appearance and composition to sample AC01 except groundmass is felted microlites of quartz and feldspar, and rock is less altered. Plagioclase phenocrysts range to as much as 7 mm in size and are zoned and twinned; some compositional zones are more altered to sericite than others. Hornblende phenocrysts are nearly completely altered to carbonate and chlorite, but in some, primary hornblende is present. Pyroxene phenocrysts are pseudomorphs of chlorite, carbonate, and iron oxide. Euhedral phenocrysts of quartz, iron oxide, apatite, and sphene are present. Groundmass alteration is sericite and chlorite with disseminated pyrite. Veinlet of carbonate is present in thin section.

Photographs:

6. 4.0-mm across; plane-polarized light. Plagioclase and hornblende in felted quartzofeldspathic groundmass.
7. Same as photograph 6 under crossed-polarized light.
8. 4.0-mm across; plane-polarized light. Carbonate veinlet approximately 0.3 mm in width.
9. 2.5-mm across; plane-polarized light. Plagioclase phenocryst, oscillatory zoned.
10. Same as photograph 9 under crossed-polarized light.
11. Same as photograph 10 in slightly different orientation.

Sample AC03

Light gray-green, highly altered, porphyritic andesite to dacite. Phenocrysts to as much as 4 mm in size of plagioclase and ferromagnesian minerals now completely altered to pseudomorphs of sericite and carbonate and sericite, iron oxide, and chlorite, respectively. A single large partially resorbed K-feldspar phenocryst may be xenocrystic. Groundmass is mostly altered to sericite, carbonate, and iron oxide. Quartz and carbonate in cavities and vugs are common.

Photographs:

12. 1.0-mm across; plane-polarized light. Pseudomorphs after plagioclase and hornblende.
13. Same as photograph 12 in crossed-polarized light.
14. 2.5-mm across; plane-polarized light. Pseudomorphs after plagioclase in altered groundmass of iron oxide, carbonate, and sericite. Vug filled with carbonate, quartz, and euhedral iron oxide.

Sample AC04

Light gray-green porphyritic andesite to dacite. Plagioclase phenocrysts, to as much as 1-cm across, are twinned oligoclase, slightly altered in zones to sericite. Hornblende is green, glassy, and euhedral with oxyhornblende rims, ranging in size to as much as 5 mm. Euhedral iron oxide to as much as 1-mm across. Approximately 1 percent pyroxene phenocrysts with alteration rims. Euhedral sphene and apatite phenocrysts compose about 1 percent of rock. Groundmass is felted quartzofeldspathic microlites. Some cavities and vugs are present.

Photographs:

15. 2.5-mm across; plane-polarized light. Phenocrysts of twinned hornblende, pyroxene, and plagioclase in quartzofeldspathic groundmass.

16. Same as photograph 15 under crossed-polarized light.

Sample AC05

Light gray-green porphyritic andesite to dacite. Plagioclase phenocrysts, to as much as 1-cm across, are twinned oligoclase, slightly altered in zones to sericite. Hornblende is green, glassy, and euhedral with oxyhornblende rims. Pyroxene phenocrysts also have oxidized rims. Groundmass is felted quartzofeldspathic microlites.

Photographs:

17. 2.5-mm across; crossed-polarized light. Phenocrysts of hornblende, pyroxene, and plagioclase in quartzofeldspathic groundmass.

18. Same as photograph 17 in plane-polarized light.

19. Same as photograph 18 under longer exposure.

Sample LU01

Light gray-green, moderately altered, porphyritic andesite to dacite. Pseudomorphed phenocrysts of plagioclase, hornblende, and pyroxene(?) in a groundmass of microlites of feldspar. Plagioclase is altered to carbonate and sericite. Ferromagnesium minerals are altered to chlorite, iron oxide, and carbonate. Fine-grained pyrite is disseminated throughout. Vugs contain zeolite(?) now altered to chlorite.

Photographs:

20. 2.5-mm across; plane-polarized light. Altered hornblende in groundmass with nearby vug of chlorite or zeolite.

21. Same as photograph 20 under crossed-polarized light.

Sample LU02

Medium gray-green porphyritic andesite to dacite. Plagioclase, hornblende, pyroxene, sphene, apatite, and iron oxide phenocrysts in a groundmass of randomly oriented quartz and feldspar microlites. Less than 1-mm wide veinlet of carbonate exposed in thin section.

Photographs:

22. 2.5-mm across; plane-polarized light. Plagioclase, hornblende, and pyroxene phenocrysts in quartzofeldspathic groundmass.

23. Same as photograph 22 under crossed-polarized light.

Sample LU03

Medium gray-green, slightly altered, porphyritic andesite to dacite. Plagioclase, hornblende, pyroxene, sphene, apatite, and iron oxide phenocrysts in a groundmass of randomly oriented quartz and feldspar microlites. Plagioclase is slightly altered in zones to sericite; hornblende has oxidized rims.

Photographs:

24. 2.5-mm across; crossed-polarized light. Phenocrysts of hornblende, pyroxene, iron oxide, and plagioclase in quartzofeldspathic groundmass.

25. Same as photograph 24 under plane-polarized light.

26. 2.5-mm across; plane-polarized light. Plagioclase, hornblende, and pyroxene phenocrysts in quartzofeldspathic groundmass.

27. Same as photograph 26 under crossed-polarized light.

28. 2.5-mm across; plane-polarized light. Phenocrysts of sphene, apatite, oxyhornblende, and quartz.

29. Same as photograph 28 in crossed-polarized light.

Sample LU04

Medium gray-green, altered, porphyritic andesite to dacite. Pseudomorphed phenocrysts of plagioclase, hornblende, and pyroxene(?) in a felted quartzofeldspathic groundmass. Plagioclase is altered to carbonate and sericite. Ferromagnesium minerals are altered to chlorite, iron oxide, and carbonate; a few have hornblende cores. Unaltered phenocrysts of sphene are present. Several 1-mm-wide carbonate veinlets are exposed in thin section.

Photographs:

30. 2.5-mm across; crossed-polarized light. Plagioclase and hornblende pseudomorphs and sphene phenocrysts in quartzofeldspathic groundmass are present.

31. Same as photograph 30 in plane-polarized light.

Sample LU05

Medium gray-green porphyritic andesite to dacite. Relatively unaltered phenocrysts of plagioclase (oligoclase to andesine to as much as 5 mm in size), acicular hornblende to 4-mm size, orthopyroxene, apatite, sphene, and fragmented quartz. Hornblende is zoned and has oxyhornblende rims. Plagioclase is slightly altered to clay and sericite. A few grains of altered K-feldspar. Groundmass is felted and quartzofeldspathic.

Photographs:

32. 2.5-mm across; plane-polarized light. Pyroxene, sphene, and oxyhornblende phenocrysts.

33. 2.5-mm across; crossed-polarized light. Alteration of plagioclase is more evident than in photograph 32.

Sample LU06

Medium gray-green, moderately altered, porphyritic andesite to dacite. Moderately altered phenocrysts of plagioclase to clay and sericite. Ferromagnesium minerals altered to iron oxides, carbonate, and chlorite; a few unaltered cores of hornblende remain. Unaltered phenocrysts of sphene and apatite are throughout. Felted quartzofeldspathic groundmass is relatively unaltered.

Photographs:

34. 2.5-mm across; plane-polarized light. Pseudomorphs of hornblende and pyroxene and moderately altered plagioclase phenocrysts.

35. Same as photograph 34 under crossed-polarized light.

Sample LU07

Medium gray-green, moderately altered, porphyritic andesite to dacite. Plagioclase phenocrysts altered to sericite. Hornblende phenocrysts altered to carbonate, sericite, and iron oxide; some remnant hornblende remains. Pyroxene phenocrysts are less altered than hornblende. Much carbonate is in the groundmass. Sphene and apatite phenocrysts are relatively unaltered. No photographs.

Sample LU08

Light gray-green porphyritic andesite to dacite. Unaltered phenocrysts of plagioclase (oligoclase), hornblende, pyroxene, sphene, and apatite in a groundmass of aligned plagioclase microlites. Plagioclase, sphene, and hornblende phenocrysts display apparent alignment.

Photograph:

36. 2.5-mm across; plane-polarized light. Aligned sphene, hornblende, and plagioclase phenocrysts.

Sample LU09

Medium gray-green, moderately altered, porphyritic andesite to dacite. Plagioclase phenocrysts are altered to masses of sericite. Ferromagnesium-mineral phenocrysts now are pseudomorphs of carbonate, chlorite, and iron oxide. Groundmass is disseminated pyrite, chlorite, and carbonate with clots of chlorite and carbonate. No photographs.

Sample LU10

Medium gray-green, moderately altered, porphyritic andesite to dacite. Plagioclase phenocrysts partly altered to sericite. Hornblende phenocrysts altered to carbonate, sericite, and iron oxide; some remnant hornblende remains. Unaltered sphene and iron oxide phenocrysts remain. Groundmass is altered to carbonate, chlorite, and iron oxide.

Photographs:

37. 2.5-mm across; plane-polarized light. Remnant hornblende core in alteration mass of chlorite, carbonate, and iron oxide.

38. Same as photograph 37 under crossed-polarized light.

Sample 60783

Light gray-green, altered, porphyritic andesite to dacite. Phenocrysts of zoned and polysynthetically twinned plagioclase are oligoclase. Plagioclase is slightly altered to sericite and carbonate. Plagioclase has an unusual mottled textural appearance that may be due to alteration or zoning. Phenocrysts of ferromagnesium minerals are completely replaced by chlorite, iron oxide, carbonate, and pyrite. Five- to 10-percent quartz in rocks appears to be spatially associated with pyrite and may be secondary. Pyrite and carbonate disseminated throughout. Unaltered apatite phenocrysts remain, but sphene phenocrysts are partly altered to iron oxide. Groundmass is now altered plagioclase consisting of carbonate and sericite.

Photographs:

39. 2.5-mm across; plane-polarized light. Patchy texture in altered plagioclase in altered groundmass.

40. Same as photograph 39 under crossed-polarized light.

41. 1.0-mm across; crossed-polarized light. Slightly altered plagioclase in mass of secondary quartz, carbonate, and sericite with disseminated pyrite.

42. Same as photograph 41 under plane-polarized light.

43. Same as photograph 42 under plane-polarized light but different exposure.

Sample 60783A

Light gray-green, altered, porphyritic andesite to dacite. Phenocrysts of zoned and polysynthetically twinned plagioclase are andesine. Phenocrysts of ferromagnesium minerals are now pseudomorphed to carbonate and chlorite. Trace of K-feldspar is found in phenocrysts. Groundmass is altered and now consists of carbonate, quartz, sericite, and pyrite.

Photographs:

44. 4.0-mm across; crossed-polarized light. Plagioclase phenocrysts in altered groundmass with <1-mm-wide quartz veinlets.

45. Same as photograph 44 under crossed-polarized light at different exposure.

46. 2.5-mm across; plane-polarized light. Slightly altered zoned plagioclase phenocrysts with cross-cutting veinlet.

47. Same as photograph 46 under cross-polarized light.

Sample 60763

Medium gray-green porphyritic andesite to dacite. Plagioclase phenocrysts are oligoclase to andesine ranging to 1-cm wide. Acicular hornblende phenocrysts are green and glassy; some have iron oxide rims. Apatite, sphene, and iron oxide phenocrysts are unaltered. Trace of K-feldspar phenocrysts. Quartz and calcite found in vugs. Groundmass is felted and quartzofeldspathic.

Photographs:

48. 2.5-mm across; plane-polarized light. Phenocrysts of K-feldspar, plagioclase, hornblende, altered pyroxene, iron oxide, and apatite.

49. Same as photograph 48 under crossed-polarized light.

Sample PI01

Light gray-green, altered, porphyritic andesite to dacite. Clots of plagioclase, quartz, and K-feldspar are slightly altered to sericite and carbonate and have a mottled character; clots are as much as 1 cm in diameter. Ferromagnesium minerals are altered to carbonate, chlorite, and white mica. Apatite phenocrysts are unaltered. Groundmass is altered to a mat of K-feldspar and carbonate with lesser amounts of quartz and sericite.

Photographs:

50. 1.0-mm across; plane-polarized light. Altered plagioclase in altered groundmass.

51. Same as photograph 50 under crossed-polarized light.

52. 4.0-mm across; crossed-polarized light. Altered plagioclase phenocrysts, white mica after pyroxene, and altered hornblende.

53. Same as photograph 52 under plane-polarized light.

54. 2.5-mm across; plane-polarized light. Large clot of altered feldspar.

55. Same as photograph 54 under crossed-polarized light.

Appendix 2. Photomicrographs

The number on upper left side of each image is the number of the photograph referred to in appendix 1.

Example:

49

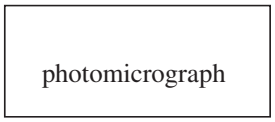

Abbreviations: ap, apatite; chl, chlorite; co, carbonate; hbl, hornblende; pl, plagioclase; py, pyrite; px, pyroxene; q, quartz; sp, sphene; wm, sericite and other white micas.

Sample AC01

1

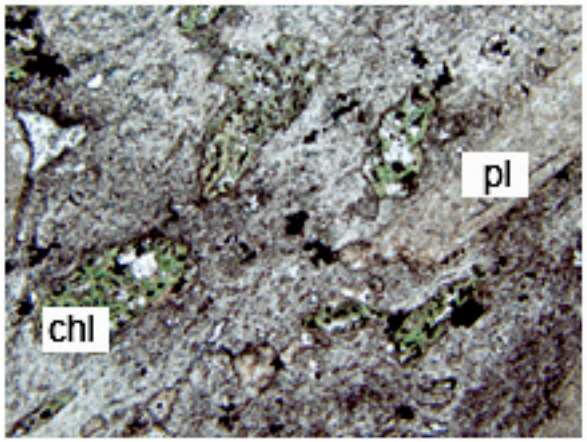

4-mm across
uncrossed polars

2

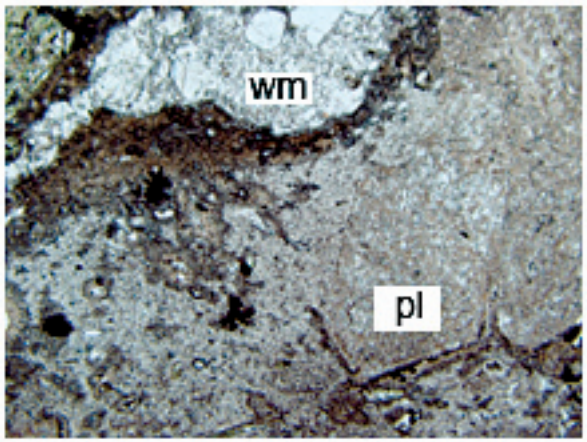

4-mm across
uncrossed polars

3

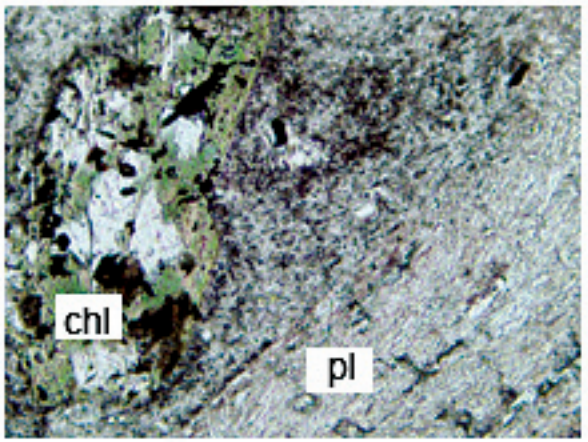

1-mm across
uncrossed polars

4

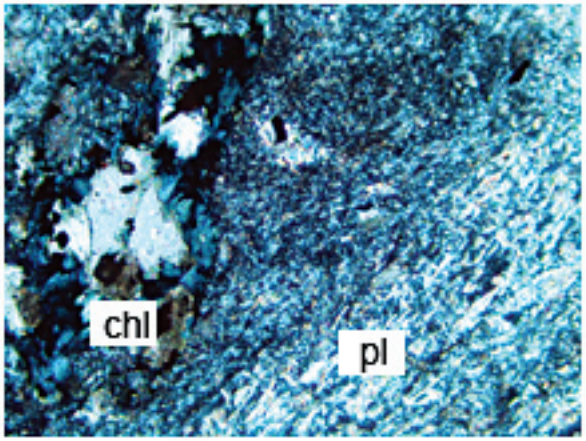

1-mm across
crossed polars

5

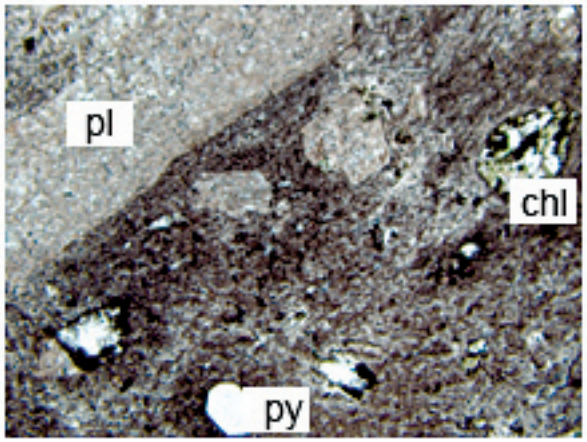

4-mm across
uncrossed polars

Sample AC02

6

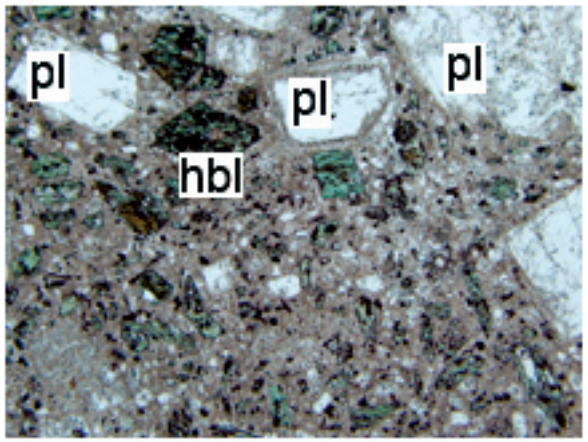

4.0-mm across
uncrossed polars

7

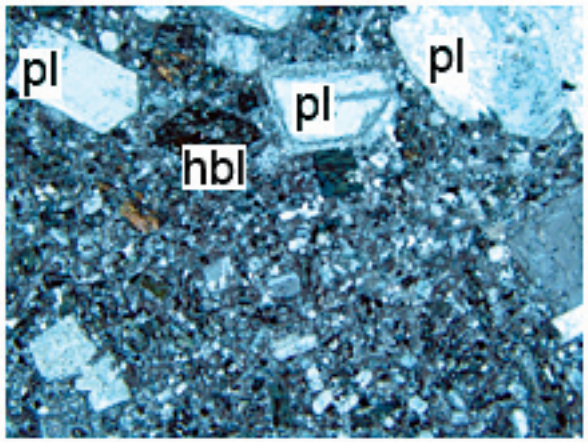

4.0-mm across
uncrossed polars

8

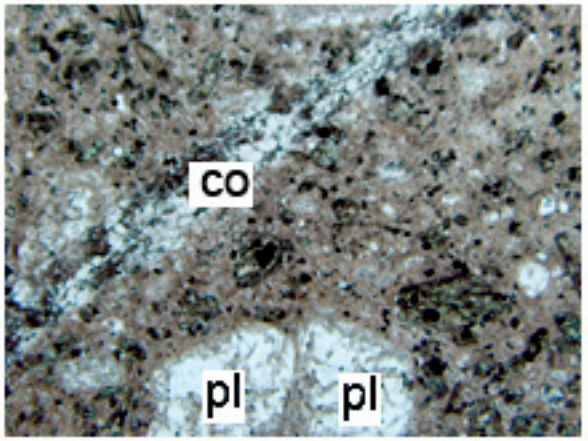

2.5-mm across
uncrossed polars

9

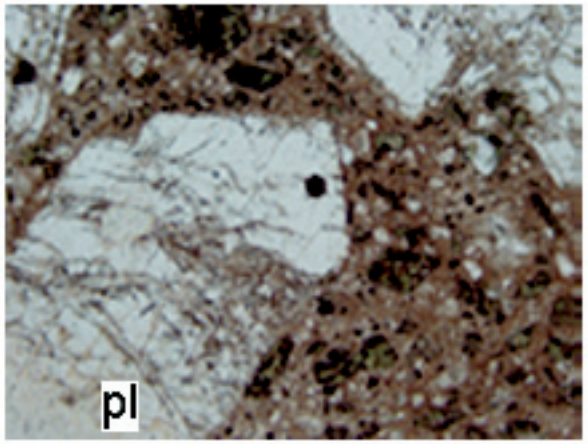

2.5-mm across
uncrossed polars

10

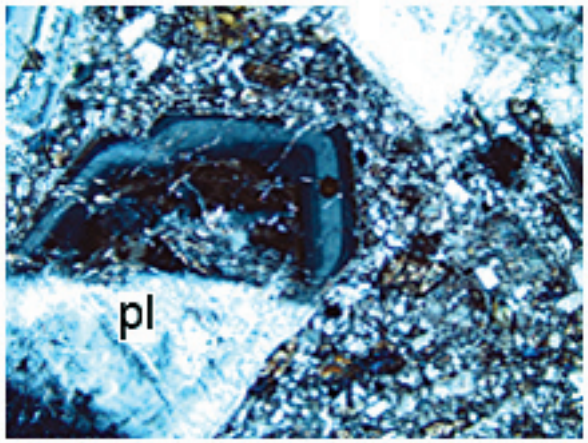

2.5-mm across
uncrossed polars

11

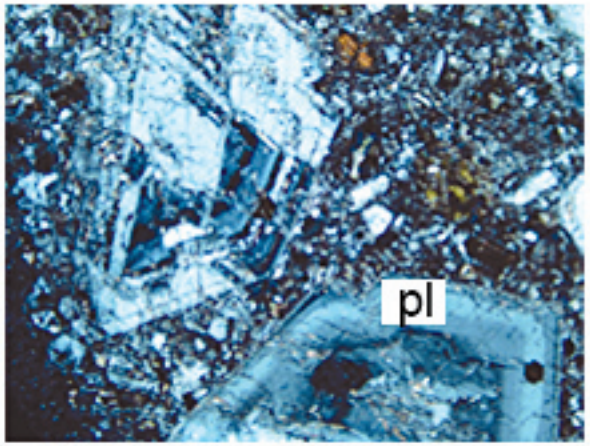

2.5-mm across
uncrossed polars

Sample AC03

12

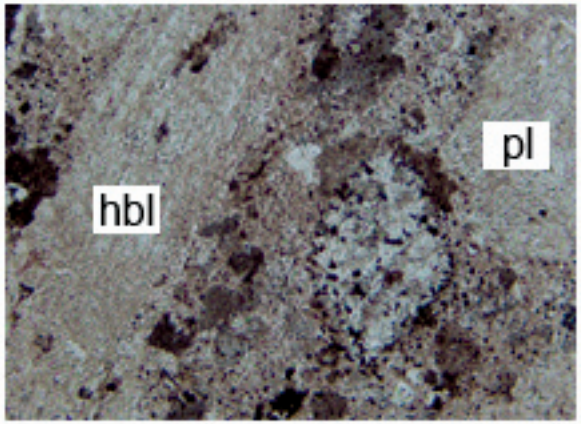

1.0-mm across
uncrossed polars

13

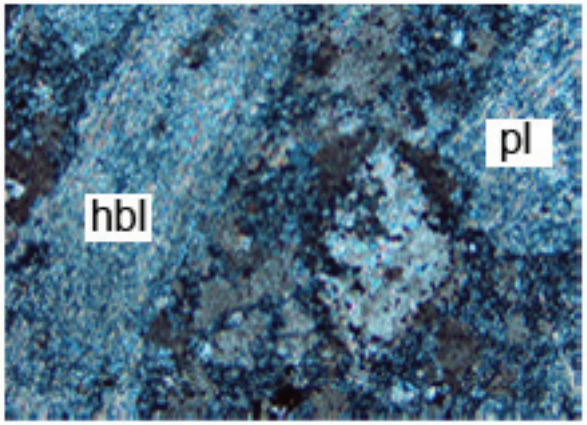

1.0-mm across
crossed polars

14

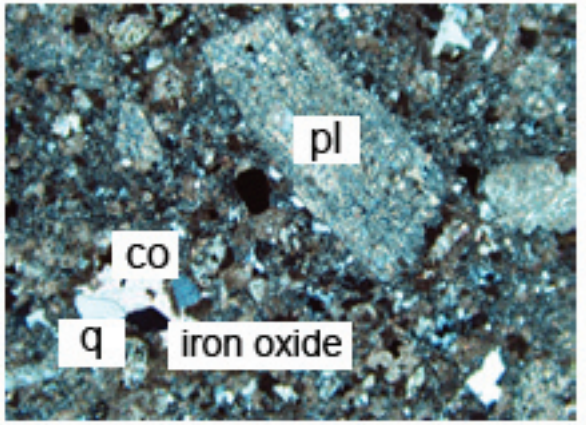

2.5-mm across
crossed polars

Sample AC04

15

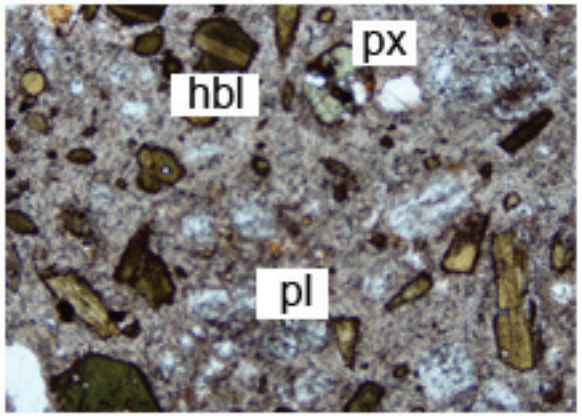

2.5-mm across
uncrossed polars

16

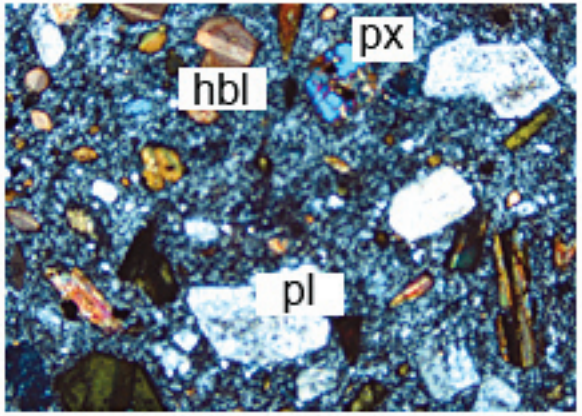

2.5-mm across
crossed polars

Sample AC05

17

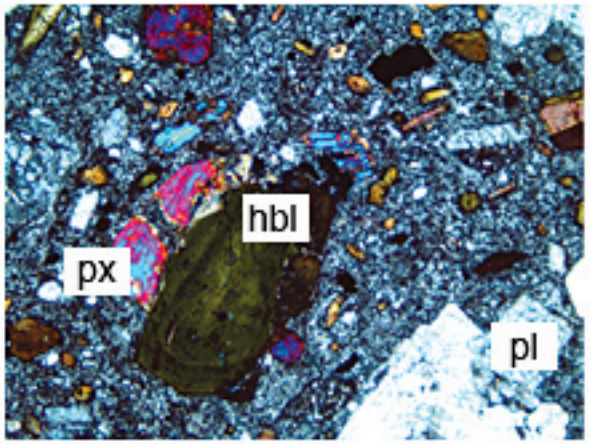

2.5-mm across
uncrossed polars

18

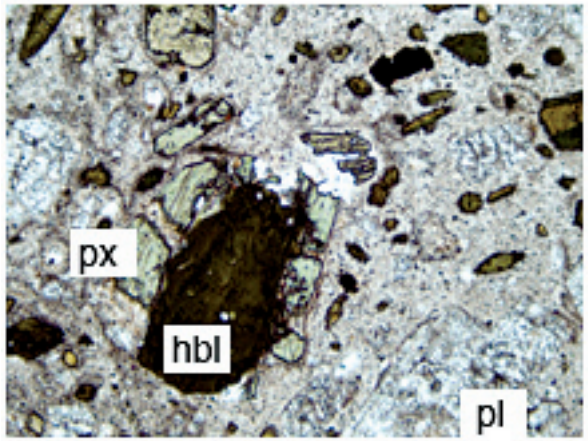

2.5-mm across
crossed polars

19

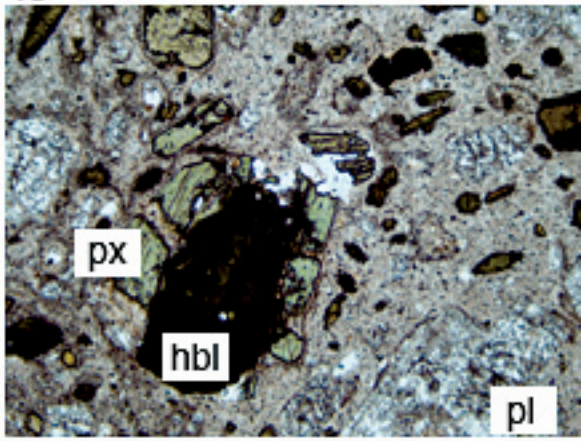

2.5-mm across
crossed polars

Sample LU01

20

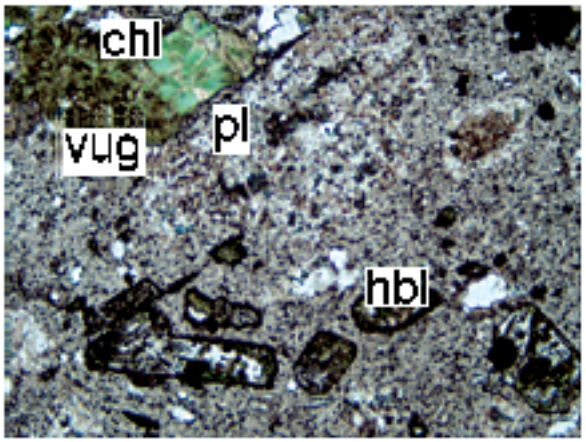

2.5-mm across
uncrossed polars

21

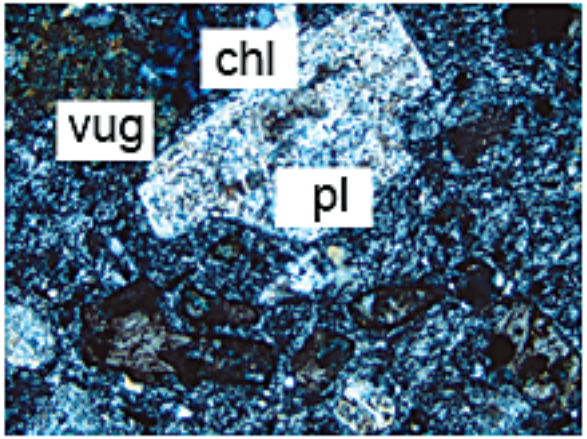

2.5-mm across
crossed polars

Sample LU02

22

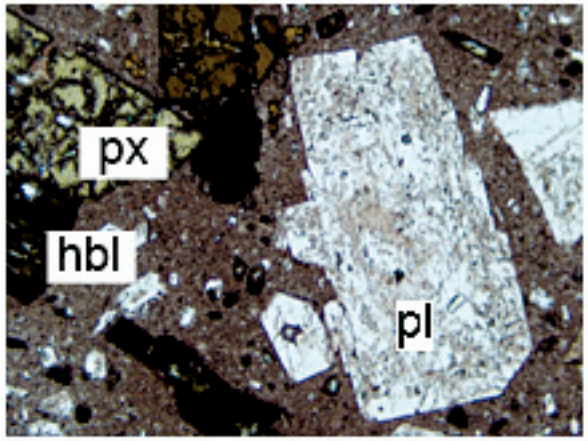

2.5-mm across
uncrossed polars

23

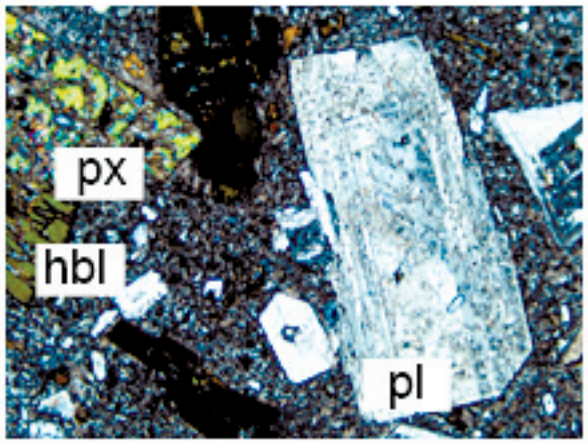

2.5-mm across
crossed polars

Sample LU03

24

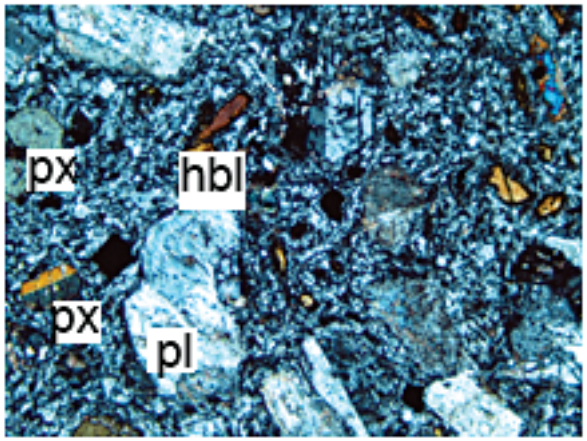

2.5-mm across
crossed polars

25

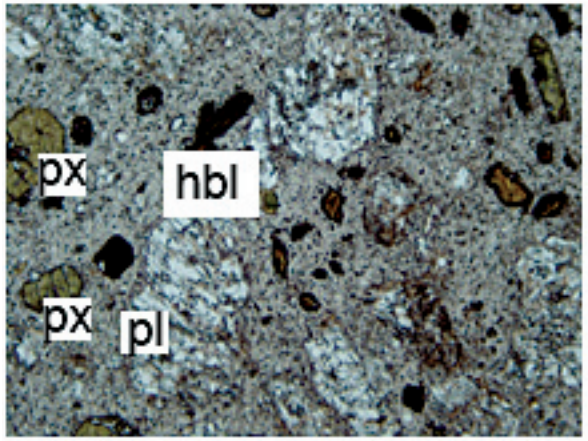

2.5-mm across
uncrossed polars

26

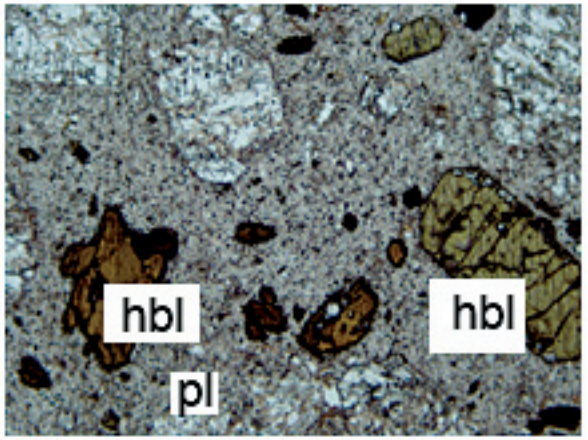

2.5-mm across
uncrossed polars

Sample LU03—Continued.

27

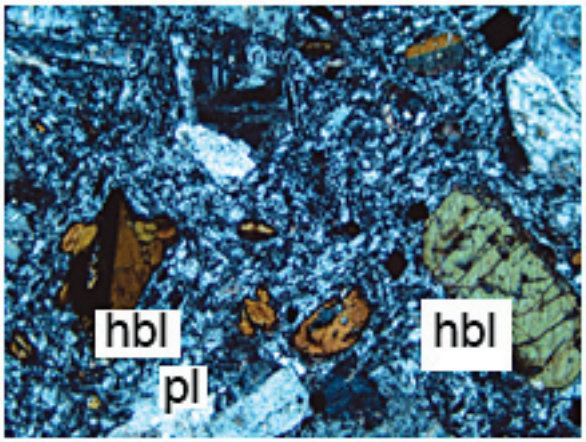

2.5-mm across
crossed polars

28

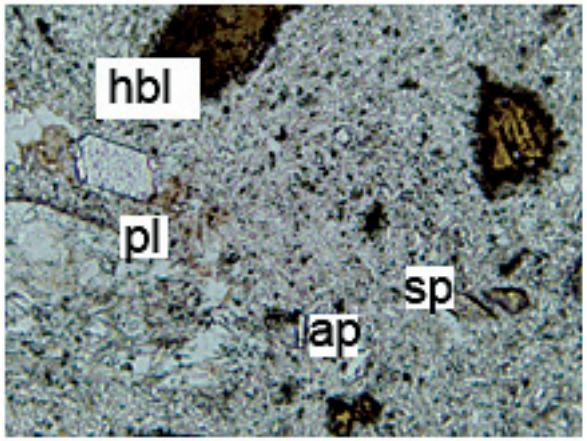

2.5-mm across
uncrossed polars

29

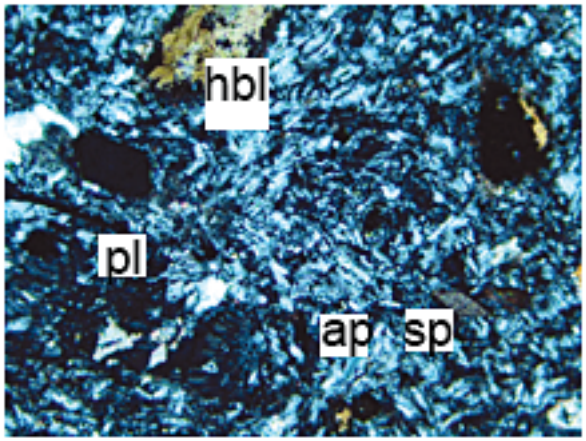

2.5-mm across
crossed polars

Sample LU04

30

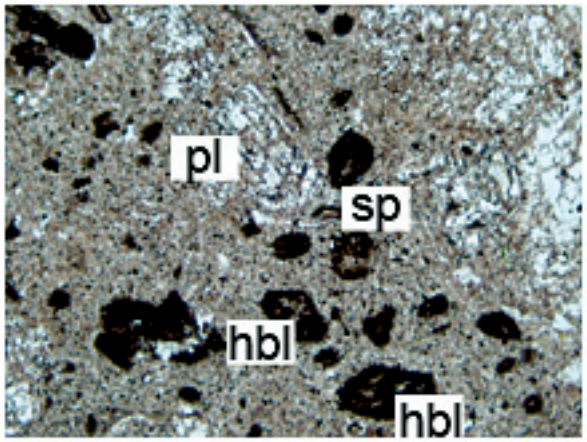

2.5-mm across
uncrossed polars

31

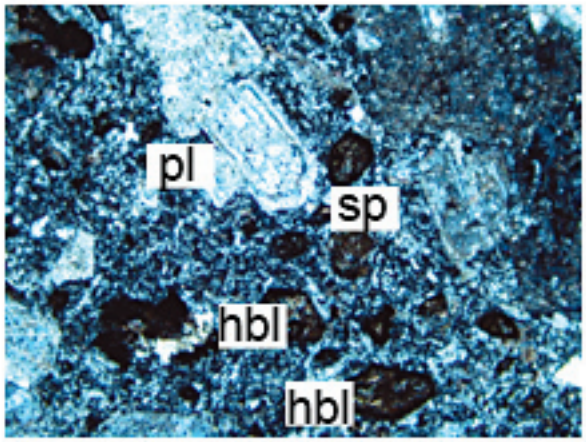

2.5-mm across
crossed polars

Sample LU05

32

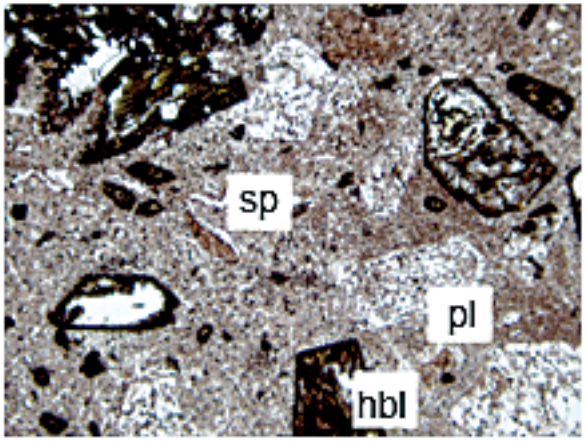

2.5-mm across
uncrossed polars

33

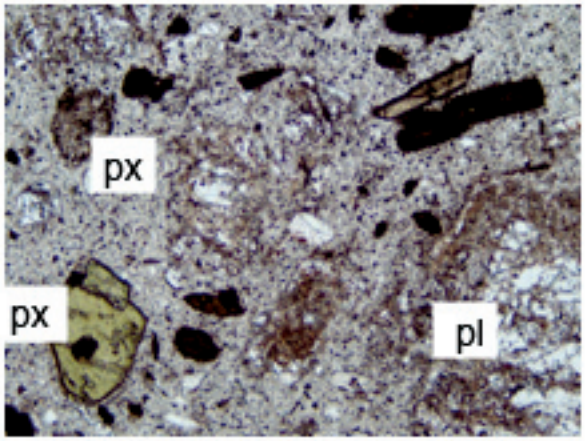

2.5-mm across
crossed polars

Sample LU06

34

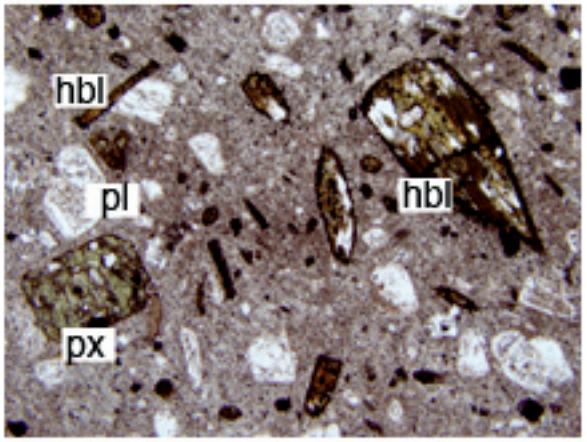

2.5-mm across
uncrossed polars

35

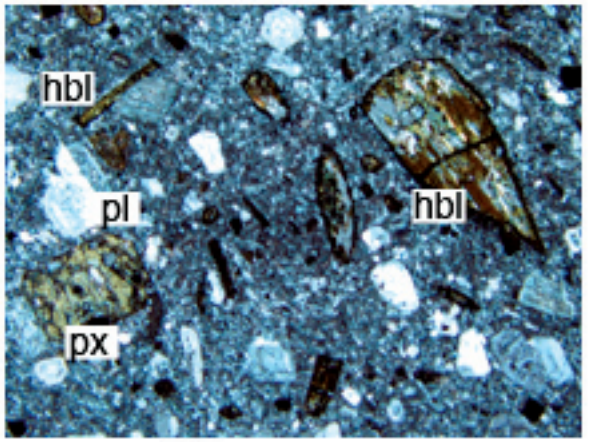

2.5-mm across
crossed polars

Sample LU08

36

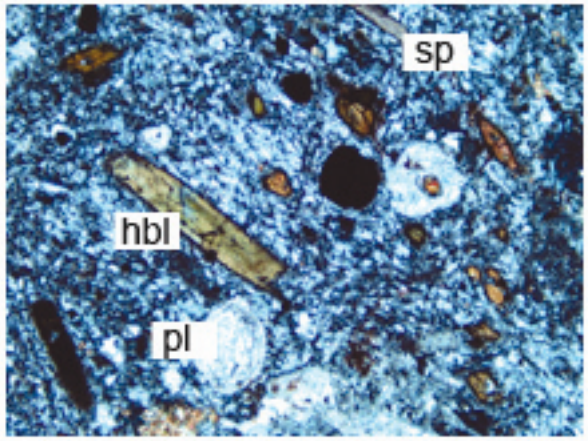

2.5-mm across
crossed polars

Sample LU10

37

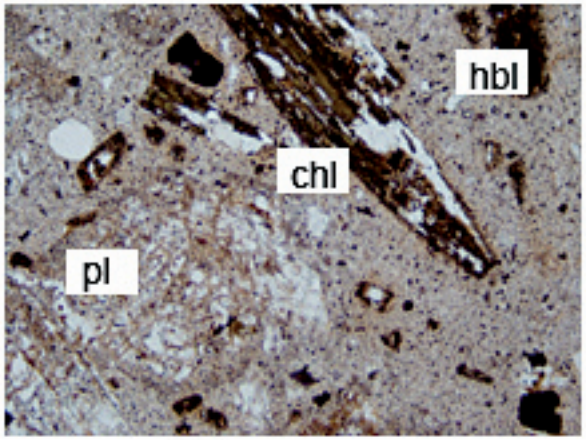

2.5-mm across
uncrossed polars

38

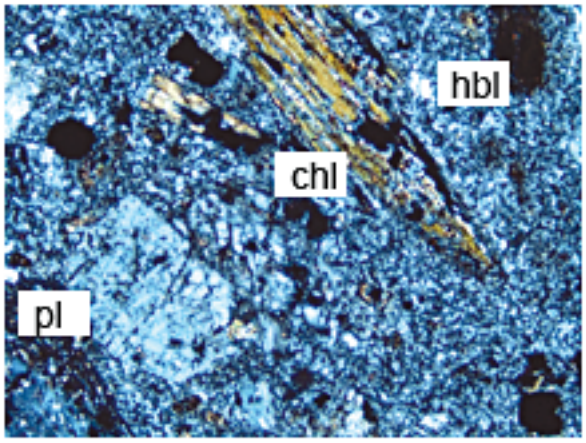

2.5-mm across
crossed polars

Sample 60783

39

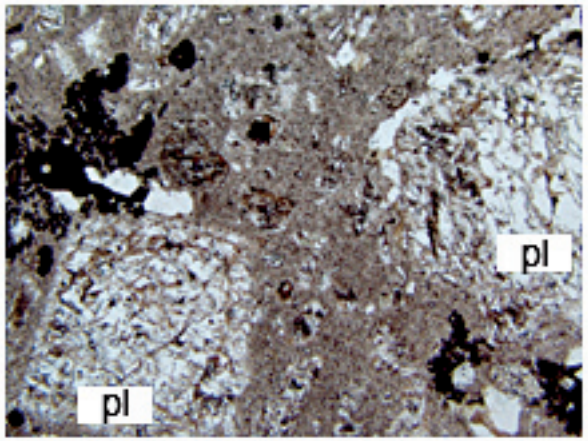

2.5-mm across
uncrossed polars

40

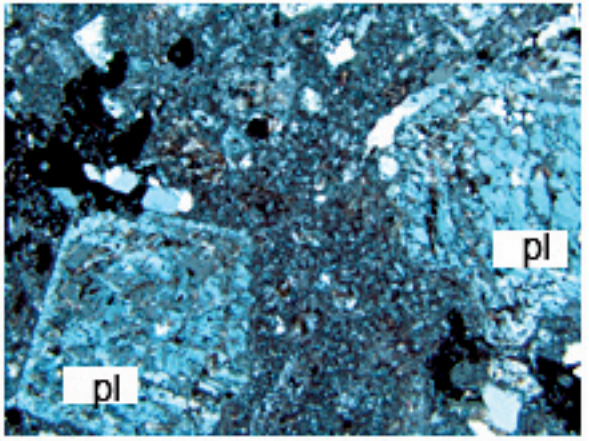

2.5-mm across
crossed polars

41

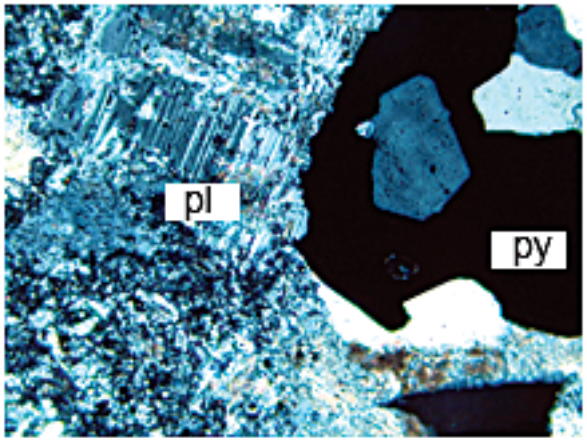

1-mm across
uncrossed polars

42

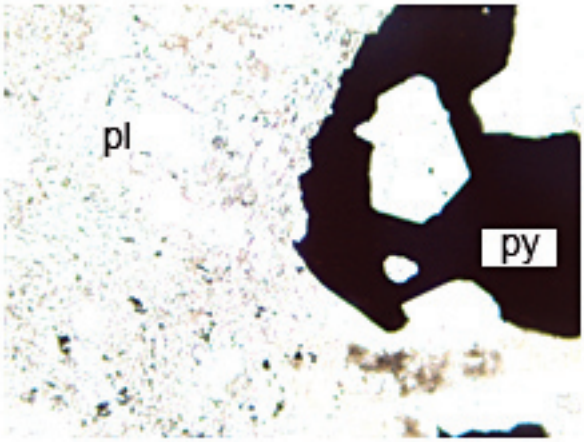

1-mm across
uncrossed polars

43

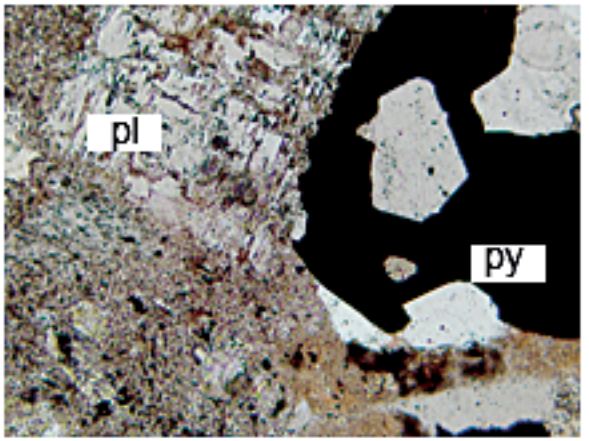

1-mm across
crossed polars

Sample 60783A

44

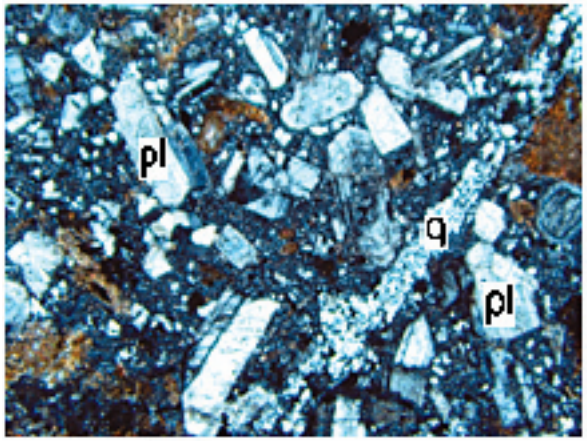

4.0-mm across
crossed polars

45

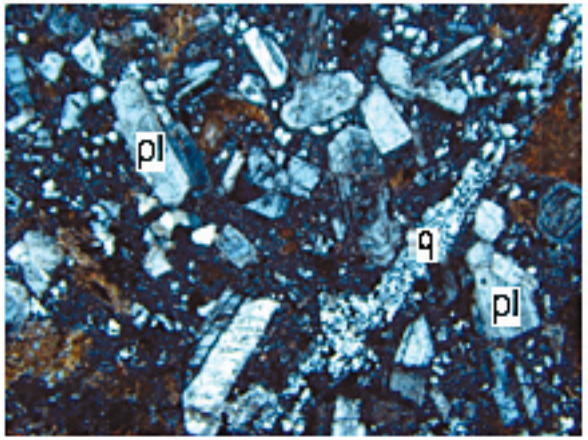

4.0-mm across
crossed polars

46

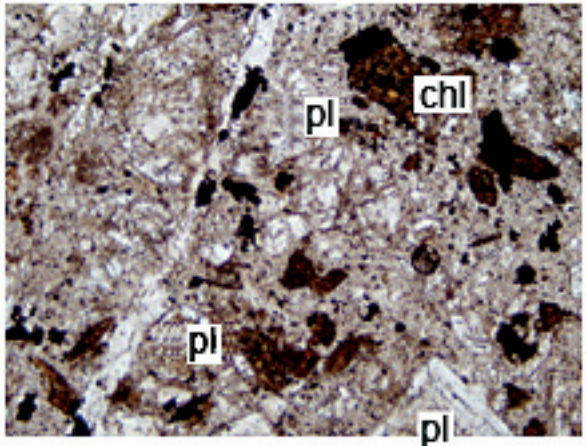

2.5-mm across
uncrossed polars

47

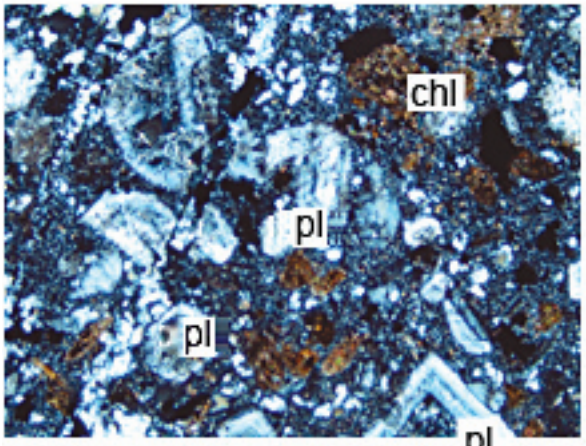

2.5-mm across
crossed polars

Sample 60763

48

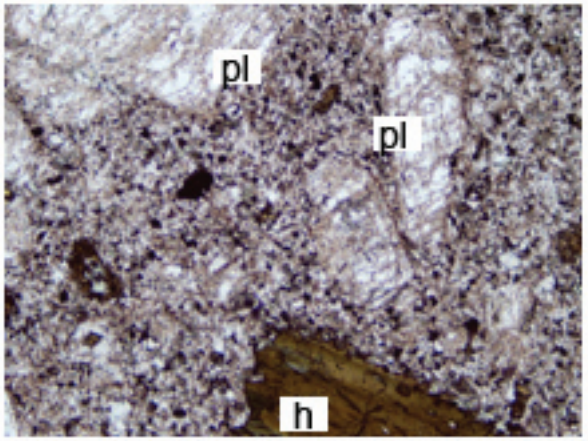

2.5-mm across
uncrossed polars

49

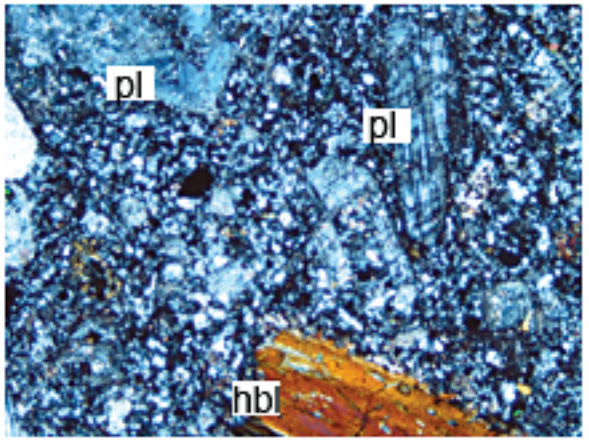

2.5-mm across
crossed polars

Sample PI01

50

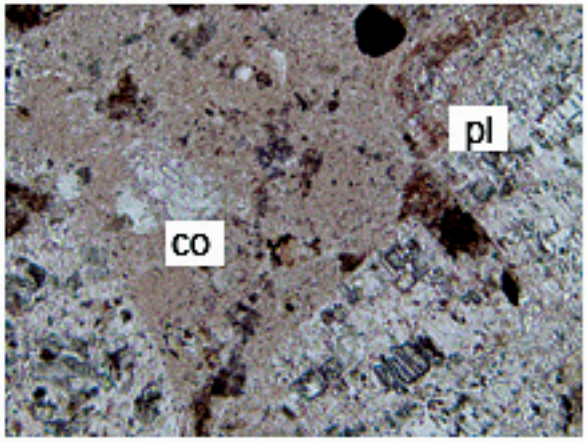

1-mm across
uncrossed polars

51

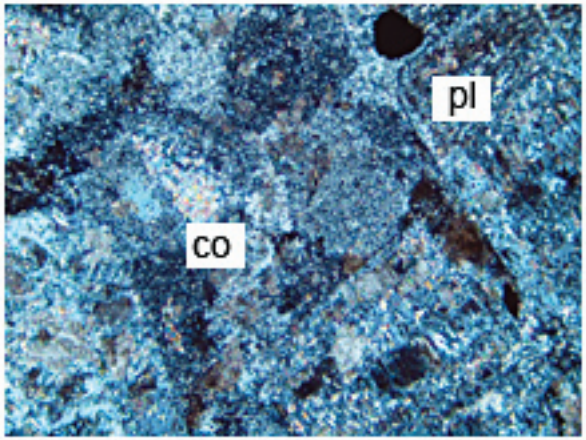

1-mm across
crosssed polars

52

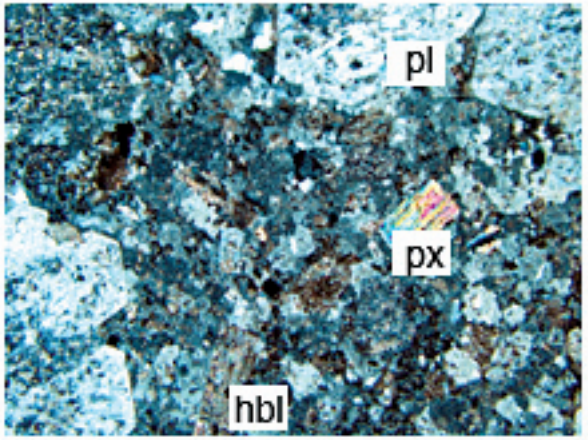

4.0-mm across
crosssed polars

Sample PI01—Continued.

53

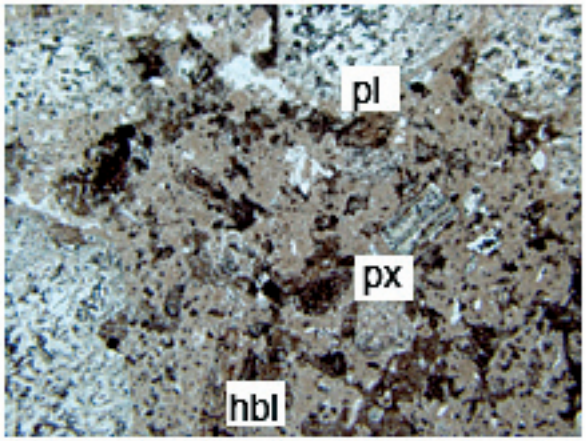

4.0 mm across
uncrossed polars

54

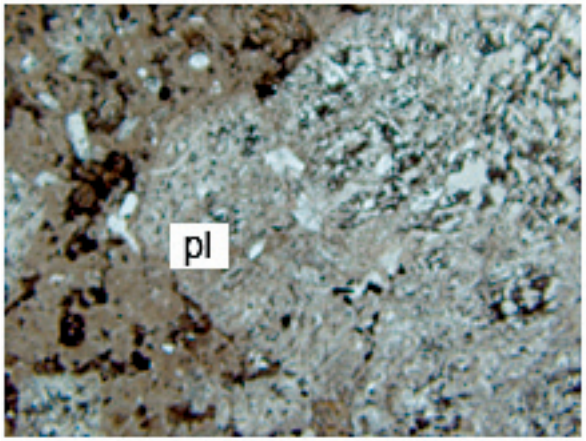

2.5-mm across
uncrossed polars

55

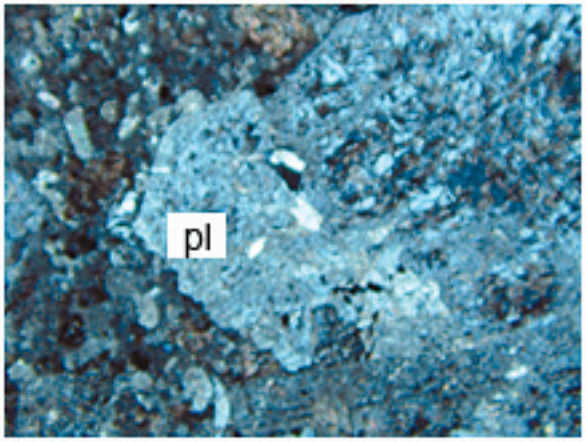

2.5-mm across
crosssed polars